

CONTROL OF A BEAM-HOVERBOARD SELF-TRANSPORTATION SYSTEM  
WITH MODEL PREDICTIVE CONTROL

A Thesis Presented

By

William R. Clark

to

The Department of Mechanical and Industrial Engineering

in partial fulfillment of the requirements  
for the degree of

Master of Science

in the field of

Mechanical Engineering

Northeastern University  
Boston, Massachusetts

May 2019

## ABSTRACT

In recent years, self-balancing transportation systems for personal use have gained increased popularity, the most popular of which being the “Hoverboard” type system. These systems function as inverted pendulum systems, with the operator acting as the pendulum, rotating a platform which incites lateral motion of a cart to maintain stability. This sort of system can be modeled as an inverted pendulum on a cart, but with the rigid pendulum replaced by a flexible cantilever beam. This allows for the vibrational characteristics to be accounted for and controlled.

In this thesis, a Model Predictive Controller (MPC) is developed to control both the stability of the flexible beam and to minimize the magnitude of the vibrations at the tip of the beam. Several theoretical MPCs are developed for multiple models of increasing complexity that represent the system simplified to different degrees; the first model is a linearized, lumped-parameter inverted pendulum on a cart, the second is a nonlinear, lumped parameter inverted-pendulum on a cart, and the third is a continuous flexible cantilever beam on a cart. Multiple models were used in order to determine the minimum amount of modelled complexity necessary to develop a controller that can adequately control the most complex system (the flexible cantilever beam).

The three controllers developed are each used in simulations with the three different models, to determine the least complex controller that can maintain the stability of the most complex model. It was found that only the controller developed specifically for the flexible beam model was able to maintain the stability, keeping the angle of the base of the beam  $<2.5 \times 10^{-3}$  rad, and the deflection in the tip of the beam  $<0.01$  m. This result is not particularly surprising, as MPCs lack robustness when dealing with model uncertainty or mismatch. This presentation concludes by discussing possible next steps for future work, including reduction of the computational load of the controller, and a design for initial experimental tests of the system.

## TABLE OF CONTENTS

Chapter 1: INTRODUCTION .....	1
1.1 Overview .....	1
1.2 Problem Background.....	1
1.2.1 Self Transportation Systems .....	1
1.2.2 Inverted Pendulum: Dynamics and Control.....	2
1.2.3 Cantilever Beam Vibration: Dynamics and Control .....	3
1.3 Model Predictive Control.....	5
1.3.1 MPC Control Structure.....	5
1.3.2 Optimization Problem and Cost Functions .....	7
1.3.3 Advantages of MPC.....	7
1.3.4 Disadvantages and potential problems .....	8
Chapter 2: Modeling and Dynamic Simulations .....	9
2.1: Proposed system.....	9
2.2: Linearized Lumped-Parameter model .....	11
2.2.1: Equations of motion .....	11
2.2.2: Dynamic simulation .....	12
2.3: Nonlinear Lumped-Parameter Model.....	14
2.3.1 Equations of motion.....	14
2.3.2 Dynamic simulation .....	15
2.4: Continuous beam system .....	16
2.4.1: Equations of motion .....	17

2.4.2: Dynamic simulations .....	20
Chapter 3: Control via MPC .....	23
3.1 Optimization Problem .....	23
3.2 Linearized Lumped-Parameter System .....	24
3.2.1 Control Design.....	24
3.2.2 Control Simulation .....	26
3.3 Nonlinear Lumped-Parameter System .....	26
3.3.1 Control Design.....	27
3.3.2 Control Simulation .....	27
3.4 Continuous system.....	28
3.4.1 Control Design.....	28
3.4.2 Controller Simulation.....	30
Chapter 4: Model Mismatch and Controller Comparison .....	31
4.1 Linear controller for nonlinear system .....	31
4.2 Linear Controller for Continuous System.....	31
4.3 Nonlinear Controller for Continuous System.....	32
Chapter 5: Conclusions and Future Work .....	33
5.1 Conclusions .....	34
5.2 Future Work .....	34
5.2.1 Explicit MPC .....	34
5.2.2 Experimental Setup.....	35
5.2.3 Lumped-Parameter Double-Beam Model.....	37
References .....	43

## LIST OF TABLES

Table 2.1: Physical Parameters of Beam-Hoverboard system.....	13
Table 3.1: MPC Parameters for Linear System .....	26
Table 3.2: MPC Parameters for Continuous System.....	29
Table 5.1: Physical Parameters of Proposed Experimental Setup.....	36

## LIST OF FIGURES

Figure 1.1: Hoverboard Self-Transportation System .....	2
Figure 1.2: Diagram of Basic Inverted Pendulum Configuration .....	3
Figure 1.3: MPC Procedure Diagram.....	6
Figure 1.4: Closed-loop MPC System Block Diagram .....	6
Figure 2.1: Design of beam-hoverboard system (left), and Coordinate systems for beam-hoverboard system (right) .....	9
Figure 2.2: Lumped-Parameter approximation of the system .....	10
Figure 2.3: Lateral position (left) and beam angle (right) of linearized beam-hoverboard system model in response to sinusoidal input $V(t) = 5 \sin t$ volts.....	13
Figure 2.4: Lateral position (left) and beam angle (right) of linearized beam-hoverboard system model in response to a step input of $V(t) = 5$ volts at $t = 1$ second.....	14
Figure 2.5: Lateral position (left) and beam angle (right) of linearized beam-hoverboard system model in response to a ramp input of $V(t) = 5t$ volts .....	14
Figure 2.6: Lateral position (left) and beam angle (right) of nonlinear beam-hoverboard system model in response to sinusoidal input $V(t) = 5 \sin t$ volts. ....	16
Figure 2.7: Lateral position (left) and beam angle (right) of linearized beam-hoverboard system model in response to a step input of $V(t) = 5$ volts at $t = 1$ second.....	16
Figure 2.8: Lateral position (left) and beam angle (right) of linearized beam-hoverboard system model in response to a ramp input of $V(t) = 5t$ volts .....	16
Figure 2.9: System Response to Sinusoidal Input $V(t) = 5 \sin t$ volts .....	21
Figure 2.10: System response to step input $V(t) = 5$ volts at $t = 1$ second .....	22
Figure 2.11: System Response to Ramp Input $V = 5t$ volts.....	22
Figure 3.1: Lateral Position (top), Beam Angle (middle), and Control Action (bottom) for Simulated Linear MPC.....	26

Figure 3.2: Lateral Position (top), Beam Angle (middle), and Control Action (bottom) for Simulated Nonlinear MPC.....	27
Figure 3.3: Continuous Beam System Closed-Loop Response with MPC .....	30
Figure 4.1: Lateral Position (top), Beam Angle (middle), and Control Action (bottom) for the Nonlinear System with a Linear Controller.....	31
Figure 4.2: Lateral Position (a), Beam Angle (b), Tip Deflection (c), and Control Action (d) for the Continuous System with a Linear Controller .....	32
Figure 4.3: Lateral Position (a), Beam Angle (b), Tip Deflection (c), and Control Action (d) for the Continuous System with a Nonlinear Controller .....	33
Figure 5.1: CAD Model of Proposed Experimental Setup .....	35
Figure 5.2: Lateral Position (a), Beam Angle (b), Tip Deflection (c), and Control Action (d) for the Proposed Experimental System .....	37
Figure 5.3: XY Plane View of Top (left) and Side (right) View of Double Beam System.....	37

## Chapter 1: INTRODUCTION

### 1.1 Overview

In recent years, self-balancing transportation systems for personal use have gained increased popularity, the most popular of which being the “Hoverboard” system. These systems are agile, compact, and effective as a mode of personal transportation in a variety of environments. However, operating them involves a certain degree of skill and physical capability, given their naturally unstable nature [1]. This presents a problem for those with physical limitations, who would benefit the most from these sorts of systems. This thesis attempts to address that, and develop a control strategy to control vibrations, and subsequently allow for easier control of these self-transportation systems by users with physical limitations.

### 1.2 Problem Background

#### 1.2.1 Self Transportation Systems

Electric self-transportation systems have become much more commonplace in recent years, ranging from larger systems like electric scooters and mopeds, to smaller and more agile systems like Segways® and Hoverboards. This has been driven by both consumer demand, as well as environmental concerns created by the prevalence of Internal Combustion Engine (ICE) technology in transportation [2]. Suppliers are attempting to meet consumer demands by balancing different aspects of these systems, such as cost, travel range, weight, and performance [3].

One type of system that has gained popularity in recent years is the Hoverboard system; this system consists of two independently rotating platforms that the operator stands on. The operator can control the speed and direction of the system by leaning forwards, backwards, or side-to-side to rotate each platform. The rotation of each platform dictates the speed of each wheel, and subsequently the direction and velocity of travel.



Figure 1.1: Hoverboard Self-Transportation System

While these systems are popular, they involve a certain degree of skill to operate. They involve a degree of balance and coordination that people with physical mobility issues may not be able to achieve. However, their size and agility make them the ideal sort of system for people with mobility issues, as current self-transportation systems designed for that group tend to be large, heavy, and not agile [4]. This creates its own problem, as people with mobility issues can have difficulty moving and maneuvering these systems in places such as the home. If a type of Hoverboard that could incorporate a degree of self-balancing to reduce the physical demand of the operator, it could be beneficial to those people with physical limitations and mobility issues.

### 1.2.2 Inverted Pendulum: Dynamics and Control

The Hoverboard systems are based on the idea of balancing an inverted pendulum. This is a well-researched problem in the area of dynamics and control. The basic concept is to keep a pendulum inverted at an unstable equilibrium point  $\theta = 0$  through the lateral motion of a cart  $x$  by applying a control input  $u$ , as shown in Figure 1.2.

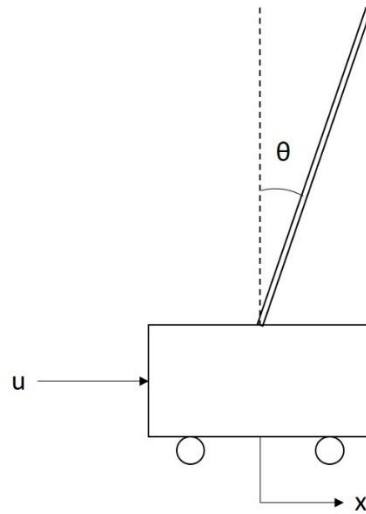


Figure 1.2: Diagram of Basic Inverted Pendulum Configuration

Much work has been done in modeling humans as inverted pendulums for transportation purposes [5-7], as well as studying the dynamics of mobile inverted pendulums [8-11]. The most common method of inverted pendulum control is the linear optimal feedback control solution [12]. This is often implemented as a Linear Quadratic Regulator (LQR), which develops a solution by solving the algebraic Riccati equation [13-14].

While linear optimal feedback is the most common solution to this problem, it is by no means the only one. The inverted pendulum problem is often used as a benchmark for testing new types of controls. As control theory has advanced, new solutions have been developed, such as using neural networks [15-16], grey model prediction [17], pseudo-state feedback [18], and sliding mode velocity control [19].

In this thesis, the system is modeled as an inverted pendulum with a flexible beam, rather than a rigid one. This makes it necessary to incorporate not only inverted pendulum controls, but also vibration and cantilever beam controls.

### 1.2.3 Cantilever Beam Vibration: Dynamics and Control

Analysis of the vibrational characteristics of flexible cantilever beams is a complex mechanical and mathematical problem. A common component of these beams that is analyzed is the deflection of the beam at a given point along the beam  $w(x, t)$ . This deflection is dependent on both the position along the beam  $x$ , and time  $t$ . There are many different analytical and numerical methods to solving this equation, including finite-element method [20], and assumed-mode method [21],

which is the method used in this thesis. This method involves using partial differential equations to break down the beam deflection into two different equations, each in terms of a single independent variable, as shown in (1.1).

$$w(x, t) = \sum_{i=1}^{\infty} W_i(x)q_i(t) \quad (1.1)$$

This equation is summed over  $i$  vibrational modes of the system, where each mode contributes a different magnitude of the vibration, based on its natural frequency, and the frequency of the vibration itself. A set of boundary conditions, both in terms of temporal and spatial limits, are also applied to solve the problem.

Much research in both mechanics and controls has been done on cantilever beam vibration. A common area of research is energy harvesting via piezoelectrics, which are a material that generate electrical charge when deformed, and deform when given electrical charge. Because of this, using them with vibrating beams is a way to generate electrical energy [22-23]. Another common application is vibration suppression and control [25-26]; this is valuable in industries such as aerospace, where it is desired to eliminate vibration from systems to ensure longevity, function, and safety.

Previous research has been conducted for the control of a cantilever beam on a cart; Ghaith et al developed a dynamic model and controller for vibration suppression of a flexible beam fixed on a moving cart using Linear Quadratic Gaussian (LQG) control strategies [27]. Nguyen et al developed a linear feedback controller to balance a flexible inverted pendulum rotating on a cart [28]. Park et al developed a mathematical model to analyze the natural frequencies and open-loop response of a flexible beam fixed on a moving cart [29]. Banavar et al used a distributed Port Hamiltonian approach to stabilize a flexible beam fixed to a cart [30], and Lin et al used piezoelectric transducers and adaptive neuro-fuzzy control to suppress vibrations of a flexible cantilever beam fixed to a cart [31].

All the past research has two distinct features in common; the system is either linearized and the linear optimal feedback control discussed previously is utilized, or the beam is fixed to the cart to prevent the base from rotating. In this thesis, the nonlinear flexible beam system is analyzed, with

rotations of the base allowed, controlled with a Model Predictive Control strategy to stabilize the system.

### 1.3 Model Predictive Control

Model predictive control (MPC), also commonly called Receding Horizon Control, is a type of control strategy that uses a predictive system model and a cost function to determine the optimal control action via an optimization algorithm to generate a desired output. This type of control originated in the late 1970s and has since become the accepted standard in the process control industry [32]. MPC describes a range of control strategies which make use of a model to find a control action by minimizing an objective function [33].

#### 1.3.1 MPC Control Structure

As stated prior, MPCs use a plant model to find an optimal control input by minimizing a user-provided function. This process is done in several steps [33-34].

- 1) The future outputs of the model are determined for a future horizon  $y(t + k)$ , where  $k = 1, 2, \dots, N$ , where  $N$  is called the prediction horizon, how far ahead in time the model outputs are calculated for, using the current model outputs at time  $t$  and a set of calculated control inputs  $u(t + l)$ , where  $l = 1, 2, \dots, M$  where  $M$  is called the control horizon, how far ahead in time the optimal control inputs are calculated for.
- 2) The next set of control inputs  $u(t + 1 + l)$  are calculated by optimizing a determined criterion to keep the model outputs  $y(t + k)$  as close to a set reference trajectory  $v(t + k)$  as possible.
- 3) The first control input of the set calculated in step 2,  $u(t + 1)$ , is implemented in the system, and the resulting output  $y(t + 1)$  is measured.
- 4) Step 1 is repeated, now with  $y(t + 1 + k)$  and  $u(t + 1 + l)$

This process is repeated as long as the system continues to run. A diagram of this control strategy is shown in Figures 1.3-1.4.

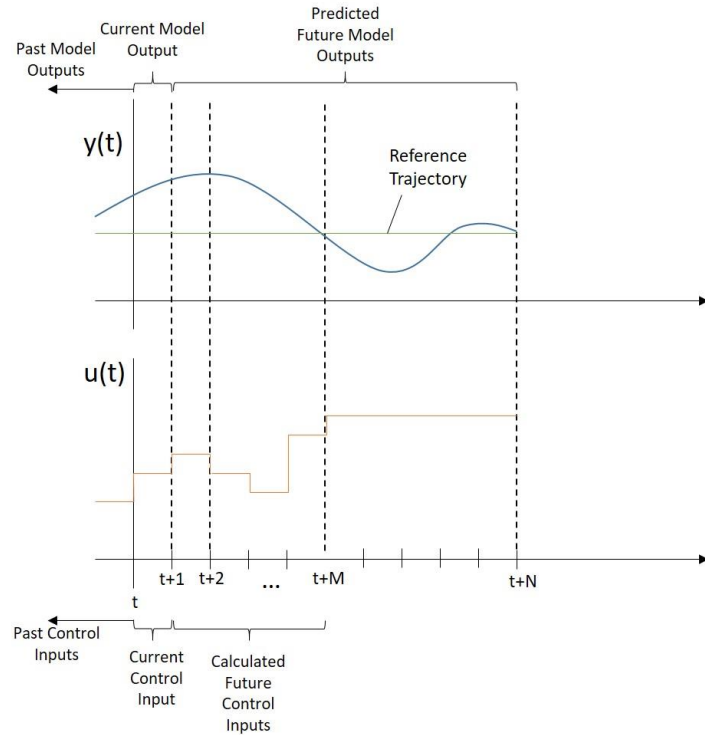


Figure 1.3: MPC Procedure Diagram

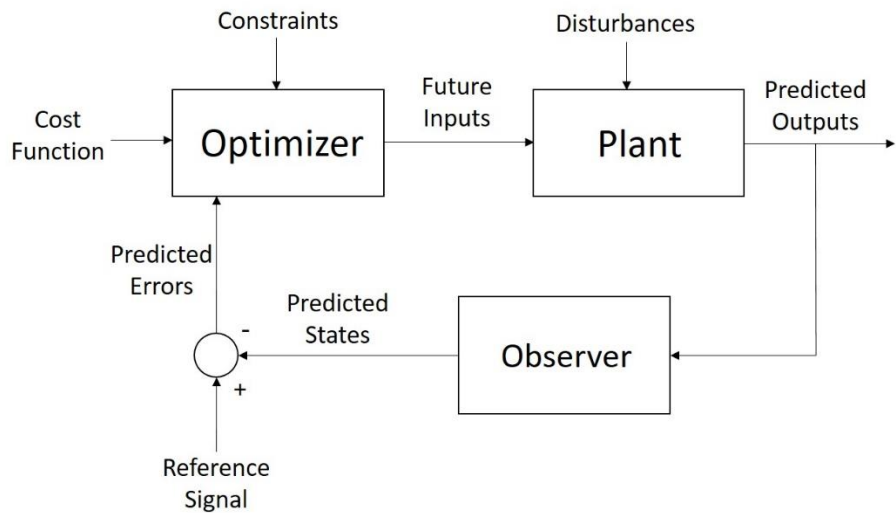


Figure 1.4: Closed-loop MPC System Block Diagram

### 1.3.2 Optimization Problem and Cost Functions

The most important part of the MPC algorithm is the optimization problem. The generalized infinite horizon optimization problem can be given by (1.2)

$$J_0^*(x(0)) = \min \sum_{k=0}^{\infty} q(x_k, u_k) \quad (1.2)$$

Where  $q(x, u)$  is the cost function, describing the user-defined “cost” of being in state  $x$  and applying input  $u$  [34], and both  $x$  and  $u$  are subject to a given set of constraints. This is an idealized version of the optimization problem, and only has an explicit solution if the system is linear (i.e.,  $x_{k+1} = Ax_k + Bu_k$ ) and unconstrained [33]. When this is the case, the optimization problem can be reduced to (1.3), and the iterations converge to a solution  $J_\infty^*(x(0)) \rightarrow P_\infty$  that satisfies the Algebraic Riccati Equation, shown in (1.4) [34].

$$J_\infty^*(x(0)) = \min_{u_1, u_2, \dots} \sum_{k=0}^{\infty} x'_k Q x_k + u'_k R u_k \quad (1.3)$$

$$P_\infty = A' P_\infty A + Q - A' P_\infty B (B' P_\infty B + R)^{-1} B' P_\infty A \quad (1.4)$$

Where  $Q$  and  $R$  are the weighting matrices for the states and inputs, respectively. This is the working solution to the LQR and linear feedback control methods discussed previously.

Outside of those conditions, a numerical approach must be used, known as receding horizon optimization, shown in (1.5)

$$J_t^*(x(t)) = \min_{u_t} p(x_{t+N}) + \sum_{k=0}^{N-1} q(x_{t+k}, u_{t+k}) \quad (1.5)$$

Where  $p(x_{t+N})$  is the terminal cost, an estimate of the state cost for  $k = N$ , and both  $x$  and  $u$  are subject to a given set of constraints.

### 1.3.3 Advantages of MPC

MPC has a number of advantages over standard control algorithms, such as their versatility and ability to be used with any model and any objective function [34], including nonlinear models [35], which proves useful in this thesis, given the highly nonlinear nature of the proposed system. MPCs can run for long periods without intervention [36], which has made them a desirable solution for industrial applications. They can also be made into adaptive controllers for use with more complex

models [37]. MPCs have also been used for inverted pendulum control [38-39], making them ideal for our application.

#### 1.3.4 Disadvantages and potential problems

There are several disadvantages to MPCs, one of which being their lack of robustness; small amounts of model uncertainty can cause major issues with MPCs [40]. There are very few schemes for robust MPC synthesis; Both Campo et al and Zheng et al show that, for a family of plants, the optimization can be recast as a linear program under specific conditions and can guarantee robust stability [41-42]. Kothare et al proposed a method of robust MPC synthesis using Linear Matrix Inequalities (LMIs), a departure from the normal robust analysis [43]. Despite this, robustness in MPCs is usually analyzed after the fact, rather than incorporated into the design. This could present issues in this thesis, as different MPC controllers will be tried with different models to determine the minimum complexity of a controller necessary to control the system model.

Another issue with MPCs is the lack of a mathematical proof to guarantee both stability and feasibility. These problems arise from the use of a finite horizon, which causes deviations between the open-loop prediction and the closed-loop system. One way to try to prove stability is to use the terminal cost in (1.5) to approximate an infinite horizon control problem, and prove that the optimal cost function is a Lyapunov function [34]. This, however, is still an estimate, and not a guarantee. Another stability proof was proposed by Kouvaritakis et al, through the use of a particular stabilizing feedback controller which replaces the relevant transfer function operators by simple polynomial operators. This, however, is limited to SISO systems [44].

## Chapter 2: Modeling and Dynamic Simulations

### 2.1: Proposed system

To account for the vibrational characteristics associated with these sorts of self-transportation systems, the following design is proposed [45]; A flexible Euler-Bernoulli cantilever beam is mounted to a platform so one end is fixed and the other is free, and a piezoelectric actuator is attached near the base of the beam. The platform has a wheel attached at each end, each of which is powered by a DC motor. This design is shown below in Figure 2.1, with the associated base (XYZ) and augmented (xyz) coordinate system [45].

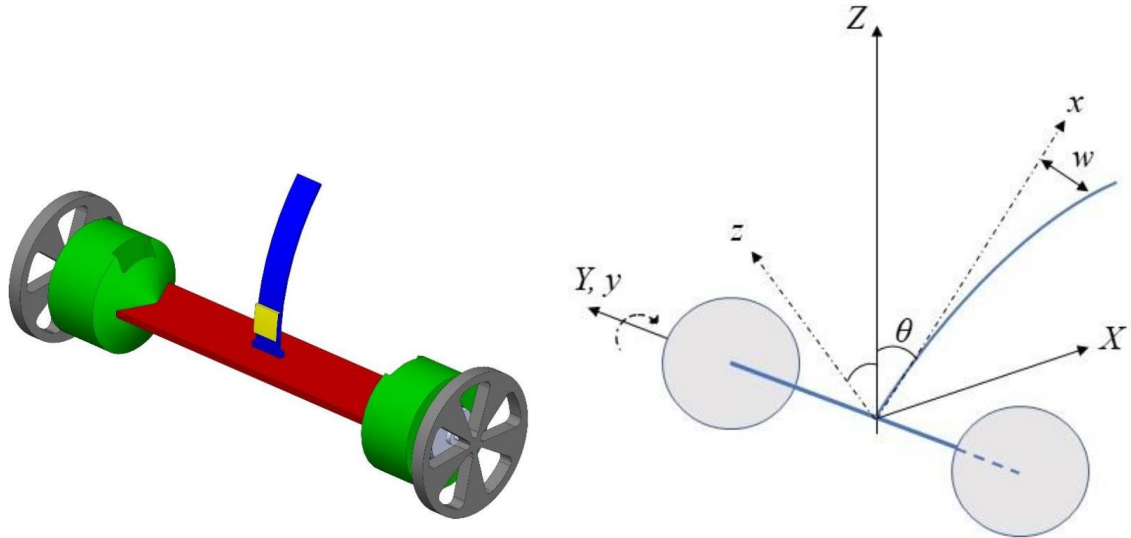


Figure 2.1: Design of beam-hoverboard system (left), and Coordinate systems for beam-hoverboard system (right)

To approximate the system as a lumped-parameter configuration, we can consider it to be a rigid massless inverted beam of length  $L$  attached to a wheel of mass  $M_w$  and radius  $r$ , with a point mass  $M$  attached to the end of the beam, as shown in Figure 2.2.

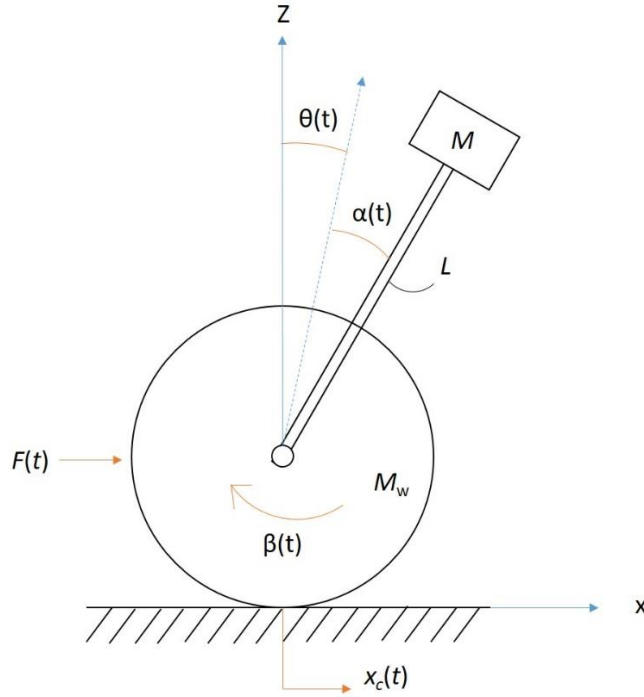


Figure 2.2: Lumped-Parameter approximation of the system

Where,  $\beta(t)$  is the angular position of the wheel,  $x_c(t)$  is the lateral position of the system along the  $X$  axis. By defining the contact between the wheel and the ground as a no-slip condition, we can also represent  $\beta(t) = x_c(t)/r$ .  $F(t)$  is the force applied to the system from the DC motor, and is given by (2.1).

$$F(t) = \frac{K_g K_t}{Rr} \left( V(t) - \frac{K_g K_m \dot{x}_c(t)}{r} \right) \quad (2.1)$$

Where  $V(t)$  is the input voltage supplied to the DC motor,  $R$  is the motor armature resistance,  $K_g$  is the internal gear ratio of the motor,  $K_m$  is the back-emf constant of the motor, and  $K_t$  is the motor torque constant.

The angle  $\theta(t)$  represents the rotation angle of the beam, while the angle  $\alpha(t)$  represents the angle that would be created by the beam deflecting due to mass  $M$  at the tip of the beam. This allows us to approximate the position of the beam tip in our lumped-parameter system separately from the rotational angle of the beam itself. The equation for  $\alpha(t)$  is given by (2.2)

$$\alpha(t) = \frac{L^2 M g}{2 G J} \sin \theta(t) \quad (2.2)$$

Where  $g$  is the acceleration due to gravity,  $G$  is the elastic modulus of the beam, and  $J$  is the second moment of area of the beam. For simplicity, we will complete the calculations using a third variable  $\gamma(t)$ , where  $\gamma(t) = \alpha(t) + \theta(t)$ .

This system will be used to develop linear and nonlinear lumped-parameter approximations of the system, and controllers will be developed for those approximations to determine the minimum complexity model that can be used as the model reference for an MPC that can control the system in Figure 2.1

## 2.2: Linearized Lumped-Parameter model

To develop the equations of motion for the linearized system, we will first develop the equations of motion for the nonlinear system, then linearize them about the working point  $\theta(t) = 0$  using small-angle approximation.

### 2.2.1: Equations of motion

To develop the equations of motion, we will use Lagrangian Mechanics given by (2.3)

$$\frac{d}{dt} \frac{\partial \mathbb{L}_I}{\partial \dot{I}} - \frac{\partial \mathbb{L}_I}{\partial I} = \Xi_I \quad (2.3)$$

Where  $\mathbb{L}$  is the Lagrangian of the system and is calculated as the difference between the kinetic and potential energy of the system,  $I$  is the set of generalized coordinates that define the system (in this case  $x_c(t)$  and  $\theta(t)$ ), and  $\Xi_I$  is the generalized forces corresponding to each generalized coordinate.

For this system, the kinetic energy is calculated from both the rotation of the wheel, rotation of the mass on the beam, the lateral motion of the wheel, and the lateral motion of the mass on the beam. This is given by (2.4)

$$\begin{aligned} T_{wm} &= \frac{1}{2} M \dot{x}_c^2(t) + \frac{1}{2} M_w \dot{x}_c^2(t) + \frac{1}{2} M L_p^2 \dot{\gamma}^2(t) + \frac{1}{2} \left( \frac{1}{2} M_w r^2 \right) \left( \frac{\dot{x}_c(t)}{r} \right)^2 \\ &= \frac{1}{2} M \dot{x}_c^2(t) + \frac{3}{4} M_w \dot{x}_c^2(t) + \frac{1}{2} M L^2 \dot{\gamma}^2(t) \end{aligned} \quad (2.4)$$

Since the potential energy of the wheel is constant in time, it can be omitted and the potential energy of the system can be taken relative to the center point of the wheel. This potential energy is given by (2.5)

$$U_b = M_w g \cos(\gamma) \quad (2.5)$$

This yields the Lagrangian shown in (2.6)

$$\mathbb{L}(x_c, \gamma) = \frac{1}{2}M\dot{x}_c^2 + \frac{3}{4}M_w\dot{x}_c^2 + \frac{1}{2}ML^2\dot{\gamma}^2 - M_wg \cos \gamma \quad (2.6)$$

The generalized forces for the system are given by the external forces applied over each generalized coordinate. In this case,  $\Xi_{x_c} = F(t) - \frac{c}{r}\dot{x}_c(t)$ , where  $c$  is a damping coefficient that represents the viscous damping of the motor shaft which opposes the rotation of the wheel, and  $\Xi_\gamma = 0$ . By applying these results to (2.3), substituting in  $\theta(t) + \alpha(t)$  for  $\gamma(t)$ , linearizing, and rearranging, the following equations of motion for the system are found.

$$\ddot{x}_c(t) = -\frac{2K_mK_tK_g^2}{3M_wRr}\dot{x}_c(t) + \frac{Mgr}{3M_w}\left(2 + \frac{L^2Mg}{GJ}\right)\theta(t) - \frac{rc(MgL^2 + 2GJ)}{3LGJM_w}\dot{\theta}(t) - \frac{2K_gK_t}{3M_wR}V(t) \quad (2.7)$$

$$\ddot{\theta}(t) = \frac{4GJK_gK_t}{3LM_wRr(MgL^2 + 2GJ)}V(t) + \frac{2c\left(M + \frac{3}{2}M_w\right)}{3L^2MM_w}\dot{\theta} + \frac{4GJK_g^2K_mK_t}{3LM_wRr^2(MgL^2 + 2GJ)}\dot{x}_c(t) - \frac{2Rgr^2\left(M + \frac{3}{2}M_w\right)}{3LM_wRr^2}\theta(t) \quad (2.8)$$

(2.7) and (2.8) represent the equations of motion of the linearized system

### 2.2.2: Dynamic simulation

To simulate the dynamics of this linear system, MATLAB can be used to simulate different input voltages to the motor and see the response of the system for a given set of parameters shown below in Table 2.1.

Table 2.1: Physical Parameters of Beam-Hoverboard System

Parameter	Symbol	Value	Unit
Mass of the wheel	$M_w$	0.1	kg
Point Mass	$M$	0.099	kg
Length of the beam	$L$	0.27	m
Radius of the wheel	$r$	0.25	m
Internal gear ratio	$K_g$	3.7:1	-
Motor torque constant	$K_t$	0.00767	Nm/Amp
Motor Armature Resistance	$R$	2.6	$\Omega$
Gravitational constant of earth	$g$	9.81	$m/s^2$
Elastic Modulus of Beam	$G$	70	GPa
Second moment of Area of Beam	$J$	$8.335 \times 10^{-7}$	$m^4$

The dynamics for (2.7) and (2.8) were with a step input, a ramp input, and a sinusoidal input, starting from an initial position of  $x_c(0) = 0$  and  $\theta(0) = 0$  (vertical). The Euler Finite Difference Method (2.9) is used to calculate the states of the model every  $dt = 0.01$  seconds.

$$X_{k+1} = X_k + \dot{X}_k dt \quad (2.9)$$

These results are shown below in Figures 2.3-2.5.

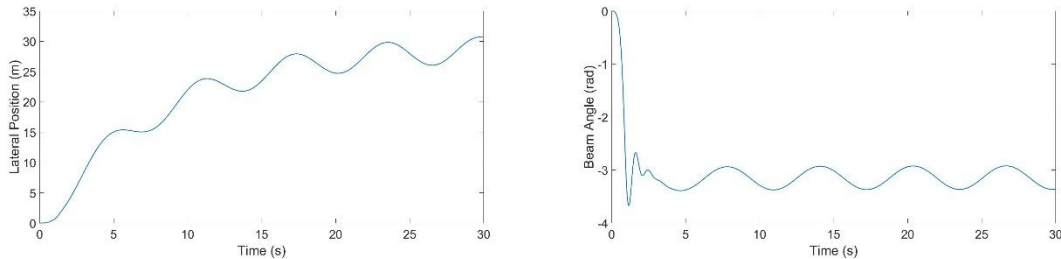


Figure 2.3: Lateral position (left) and beam angle (right) of linearized beam-hoverboard system model in response to sinusoidal input  $V(t) = 5 \sin t$  volts

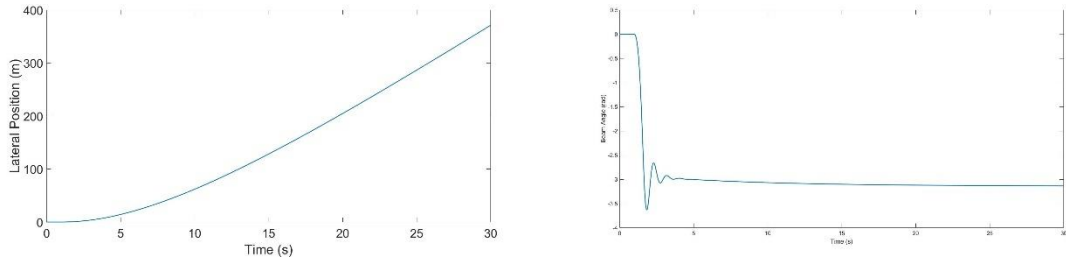


Figure 2.4: Lateral position (left) and beam angle (right) of linearized beam-hoverboard system model in response to a step input of  $V(t) = 5$  volts at  $t = 1$  second

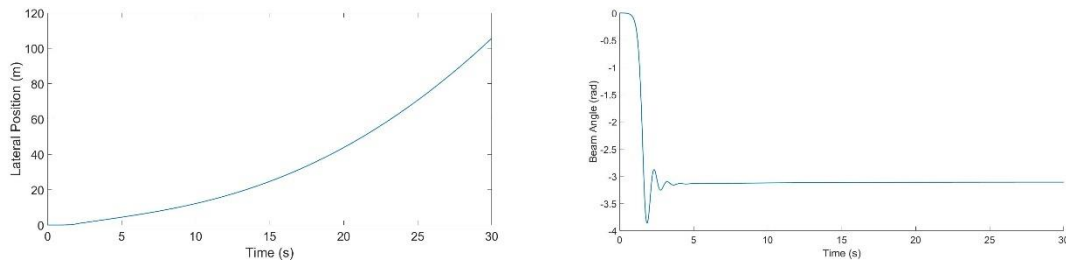


Figure 2.5: Lateral position (left) and beam angle (right) of linearized beam-hoverboard system model in response to a ramp input of  $V(t) = 5t \leq 5$  volts

These results are the expected results from this system, where  $x_c(t)$  continues increasing for any positive input, and decreases for any negative input, while  $\theta$  initially decreases to  $-\pi$  radians, and oscillates until it reaches equilibrium. This represents the beam falling backwards in response to a forward motion of the cart, until it reaches its most downward position.

### 2.3: Nonlinear Lumped-Parameter Model

The nonlinear lumped-parameter model is similar to the linear model, but it does not linearize the system about the working point  $\theta = 0$ .

#### 2.3.1 Equations of motion

The equations of motion for the nonlinear model are derived in the same manner as (2.7) and (2.8) in the linear model, but the results of the operations on (6) are not linearized. This results in (2.10) and (2.11) below.

$$\begin{aligned}
& \left( M \sin^2 \left( \frac{MgL^2 \sin \theta(t) + 2GJ\theta(t)}{2GJ} \right) + \frac{3}{2} M_w \right) \ddot{x}_c(t) \\
&= \frac{K_g K_t}{rR} V(t) \\
&+ \left( \frac{c}{L} + \frac{LMcg}{2GJ} \cos \theta(t) \right) \cos \left( \frac{MgL^2 \sin \theta(t) + 2GJ\theta(t)}{2GJ} \right) \dot{\theta}(t) \\
&+ \left( LM + \frac{L^5 M^3 R g^2}{4G^2 J^2} \cos^2 \theta(t) \right. \\
&\quad \left. + \frac{L^3 M^2 g}{GJ} \cos \theta(t) \right) \sin \left( \frac{MgL^2 \sin \theta(t) + 2GJ\theta(t)}{2GJ} \right) \dot{\theta}^2(t) \\
&- \frac{K_g^2 K_m K_t}{r^2 R} \dot{x}_c(t) - \frac{1}{2} Mg \sin \left( \frac{MgL^2 \sin \theta(t) + 2GJ\theta(t)}{GJ} \right)
\end{aligned} \tag{2.10}$$

$$\begin{aligned}
& - \frac{1}{2} L(MgL^2 \cos \theta(t) + 2GJ)(2M \sin^2 \left( \frac{MgL^2 \sin \theta(t) + 2GJ\theta(t)}{2GJ} \right) + 3M_w) \ddot{\theta}(t) \\
&= c \left( gL \cos \theta(t) + \frac{2GJ}{LM} \right) \dot{\theta}(t) \\
&+ \frac{2GJ}{M + \frac{3}{2} M_w} \cos \left( \frac{MgL^2 \sin \theta(t) + 2GJ\theta(t)}{2GJ} \right) \left( \frac{K_g K_t}{rR} V(t) \right. \\
&\quad \left. - \frac{K_g^2 K_m K_t}{r^2 R} \dot{x}_c(t) \right) \\
&+ \left( \frac{L^3 M^2 g \sin \theta(t)}{M + \frac{3}{2} M_w} \cos^2 \left( \frac{MgL^2 \sin \theta(t) + 2GJ\theta(t)}{2GJ} \right) - LM \sin \theta(t) \right. \\
&\quad \left. + \frac{LM(MgL^2 \cos \theta(t) + 2GJ)^2}{2GJ \left( M + \frac{3}{2} M_w \right)} \tan \left( \frac{MgL^2 \sin \theta(t) + 2GJ\theta(t)}{2GJ} \right) \right) \dot{\theta}^2(t) \\
&- 2GJg \sin \left( \frac{MgL^2 \sin \theta(t) + 2GJ\theta(t)}{2GJ} \right)
\end{aligned} \tag{2.11}$$

### 2.3.2 Dynamic simulation

The same simulations are conducted for the linearized system are conducting here, using the same inputs, finite difference approach, and physical parameters. The results are shown in Figures 2.6-2.8

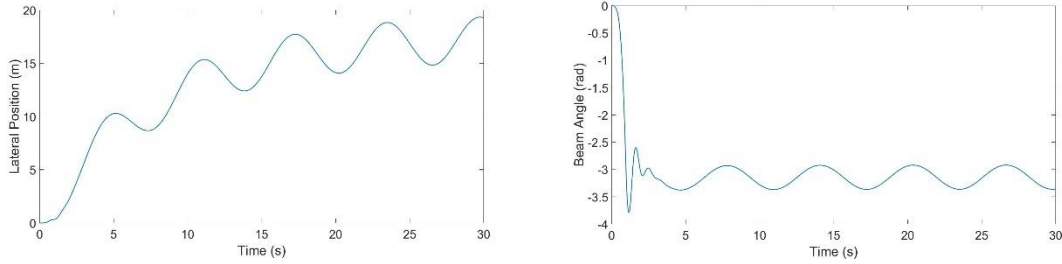


Figure 2.6: Lateral position (left) and beam angle (right) of nonlinear beam-hoverboard system model in response to sinusoidal input  $V(t) = 5 \sin t$  volts.

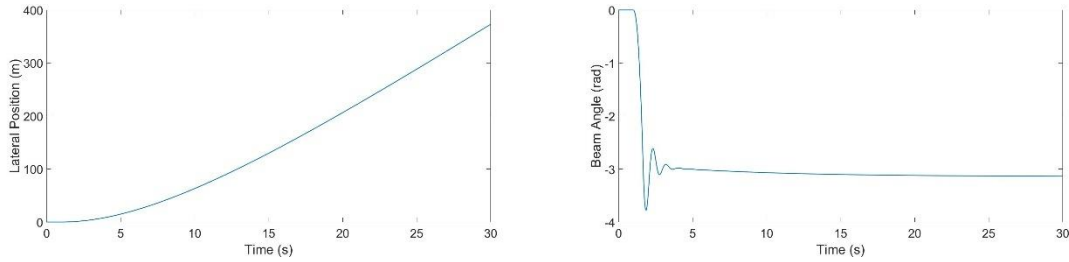


Figure 2.7: Lateral position (left) and beam angle (right) of linearized beam-hoverboard system model in response to a step input of  $V(t) = 5$  volts at  $t = 1$  second.

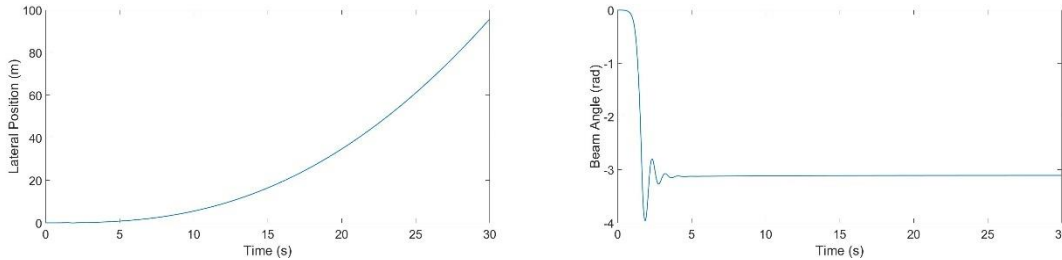


Figure 2.8: Lateral position (left) and beam angle (right) of linearized beam-hoverboard system model in response to a ramp input of  $V(t) = 5t$  for  $t \leq 5$  volts

These results closely match the linearized results, which is expected as the linear model is a good approximation for the nonlinear model.

## 2.4: Continuous beam system

The results in this chapter have been previously published by the author in Proceedings of ASME 2018 Dynamic System and Control Conference [45].

To calculate the equations of motion of the continuous beam system, the Lagrangian approach used previously cannot be used, due to the continuous nature of the system. Instead, the Extended Hamilton's Principle will be used (2.12)

$$\delta \int_{t_1}^{t_2} (T_b + T_{wm} - U_b + W^{ext} + W^{nc}) dt = 0 \quad (2.12)$$

Where  $T_b$  is the kinetic energy of the beam,  $T_{wm}$  is the kinetic energy of the wheels,  $U_b$  is the potential energy of the beam,  $W^{ext}$  is the work done by external forces, and  $W^{nc}$  is the non-conservative work of the system.

#### 2.4.1: Equations of motion

$T_b$  can be found from the velocity of each portion of mass of the beam,  $V_b$  (2.13)

$$V_b^2 = (\dot{x}_c(t) + x\dot{\theta}(t)\cos\theta(t) + w_t(x, t)\cos\theta(t) - w(x, t)\dot{\theta}(t)\sin\theta(t))^2 + (\dot{x}\dot{\theta}(t)\sin\theta(t) - w_t(x, t)\sin\theta(t) - w(x, t)\dot{\theta}(t)\cos\theta(t))^2 \quad (2.13)$$

$$T_b = \frac{1}{2} \int_0^L \rho A \left( (\dot{x}_c(t) + x\dot{\theta}(t)\cos\theta(t) + w_t(x, t)\cos\theta(t) - w(x, t)\dot{\theta}(t)\sin\theta(t))^2 + (\dot{x}\dot{\theta}(t)\sin\theta(t) - w_t(x, t)\sin\theta(t) - w(x, t)\dot{\theta}(t)\cos\theta(t))^2 \right) dx \quad (2.14)$$

Where  $x$  is the position along the length of the beam,  $w(x, t)$  is the deflection of position  $x$  along the beam at time  $t$ ,  $\rho$  is the system density, and  $A$  is the cross-sectional area of the system.

It should be noted that, due to the piezoelectric actuator described in section 2.1,  $\rho A$  is not constant the entire length of the beam (2.15)

$$\rho A = \begin{cases} \rho_b A_b + \rho_p A_p & x \leq L_p \\ \rho_b A_b & x > L_p \end{cases} \quad (2.14)$$

Where,  $\rho_b$  is the density of the beam,  $\rho_p$  is the density of the piezoelectric actuator,  $A_b$  is the cross-sectional area of the beam,  $A_p$  is the cross-sectional area of the piezoelectric actuator, and  $L_p$  is the length of the piezoelectric actuator.

The potential energy of the beam variations,  $\delta U_b$ , can be written as (2.15)

$$\delta U_b = \int_0^L \rho A g (-\sin\theta(t) \delta w - (w(x, t) \cos\theta(t) + x \sin\theta(t)) \delta\theta) + \left( EI w_{xx}(x, t) + z_p d_{31} S(x) \frac{v(t)}{t_p} \right) dx \quad (2.15)$$

where  $z_p$  defines the neutral axis along the Z-axis,  $d_{31}$  is the piezoelectric constant of the actuator,  $v(t)$  is voltage applied to the piezoelectric actuator,  $t_p$  is the thickness of the piezoelectric actuator, and  $EI$ , similar to  $\rho A$ , is expressed as

$$EI = \begin{cases} E_b I_b + E_p I_p & x \leq L_p \\ E_b I_b & x > L_p \end{cases} \quad (2.16)$$

Where  $E_b$  and  $E_p$  are the Young's moduli of elasticity of the beam and the piezoelectric, respectively, and  $I_b$  and  $I_p$  denote the mass moments of inertia of the beam and piezoelectric cross-section about the Y-axis, and  $S(x) = H(x) - H(x - L_p)$ , where  $H(x)$  is the Heaviside Function.

The work done by external forces can be represented by (2.17)

$$\delta W^{ext} = F(t) \delta x_c = \frac{K_g K_t}{Rr} \left( V(t) - \frac{K_g K_m \dot{x}_c(t)}{r} \right) \delta x_c \quad (2.17)$$

And the non-conservative work of the system is due to the viscous damping of the beam, and of the motor shaft, and can be represented by (2.18)

$$\delta W^{nc} = -C w_t \delta w - c \frac{\dot{x}_c}{r^2} \delta x_c \quad (2.18)$$

In order to solve (2.12), further analysis of  $w(x, t)$  is required. To do this, it will be assumed that the beam is unforced, undamped, and has harmonic motion with frequency  $\omega$ . This will allow  $w(x, t)$  to be rewritten as (2.19).

$$w(x, t) = W(x) e^{i\omega t} \quad (2.19)$$

With

$$W(x) = a_1 \cos \beta x + a_2 \sin \beta x + a_3 \cosh \beta x + a_4 \sinh \beta x \quad (2.20)$$

$$\omega_r = \beta_r^2 \sqrt{\frac{EI}{\rho A}} \quad (2.21)$$

By assuming the beam is unforced and undamped, the following boundary conditions can be applied

$$\rho A w_{tt} + \frac{\partial(EI w_{xx})}{\partial x^2} = 0 \quad (2.22)$$

$$\begin{cases} w(0, t) = 0 \\ w_x(0, t) = 0 \\ w_{xx}(L, t) = 0 \\ w_{xxx}(L, t) = 0 \end{cases} \quad (2.23)$$

Substituting (2.20) into (2.23) yields

$$W(x) = \sum_{r=1}^{\infty} \frac{\cosh \beta_r L + \cos \beta_r L}{\sin \beta_r L - \sinh \beta_r L} (\cosh \beta_r x - \cos \beta_r x) + \sinh \beta_r x - \sin \beta_r x \quad (2.24)$$

From there, assumed mode method (AMM) expansion technique can be used to expand  $w(x, t)$  into a partial differential equation of the form

$$w(x, t) = \sum_{i=1}^{\infty} W_i(x) q_i(t) \quad (2.25)$$

By substituting (2.25), (2.18), (2.17), (2.15), (2.14) and (2.4) into (2.12), and applying the boundary conditions from (2.22) and (2.23), the equations of motion for this system can be found, as shown in (2.26) – (2.28) [45].

$$\begin{aligned} & \left( \ddot{q}_i(t) - \dot{\theta}^2(t) \right) \int_0^L \rho A W_i^2(x) dx + \dot{q}_i(t) \int_0^L C W_i^2(x) dx + q_i(t) \int_0^L G J W_{ixx}^2(x) dx \\ & + \ddot{\theta}(t) \int_0^L \rho A x W_i(x) dx \\ & + (\ddot{x}_c(t) \cos \theta(t) - g \sin \theta(t)) \int_0^L \rho A W_i(x) dx \\ & + \left( \frac{z_p d_{31} E_p v(t)}{t_p} \right) \int_0^L S(x) W_{ixx}(x) dx = 0 \rightarrow i = 1, 2, \dots \end{aligned} \quad (2.26)$$

$$\begin{aligned}
& \ddot{x}_c(t) \left( 2 \left( M_w + \frac{I_w}{r} \right) + \int_0^L \rho A dx \right) + \cos \theta(t) \sum_{i=1}^{\infty} \ddot{q}_i(t) \int_0^L \rho A W_i(x) dx \\
& + \ddot{\theta}(t) \left( \cos \theta(t) \int_0^L \rho A x dx - \sin \theta(t) \sum_{i=1}^{\infty} q_i(t) \int_0^L \rho A W_i(x) dx \right) \\
& - \dot{\theta}(t) \left( \sin \theta(t) \sum_{i=1}^{\infty} \dot{q}_i(t) \int_0^L \rho A W_i(x) dx \right) \\
& - \dot{\theta}^2(t) \left( \sin \theta(t) \int_0^L \rho A x dx + \cos \theta(t) \sum_{i=1}^{\infty} q_i(t) \int_0^L \rho A W_i(x) dx \right) \\
& = 2 \frac{K_g K_t}{Rr} \left( V(t) - \frac{K_g K_m \dot{x}_c(t)}{r} \right)
\end{aligned} \tag{2.27}$$

$$\begin{aligned}
& \ddot{x}_c \left( \cos \theta(t) \int_0^L \rho A x dx - \sin \theta(t) \sum_{i=1}^{\infty} q_i(t) \int_0^L \rho A W_i(x) dx \right) \\
& + \ddot{\theta}(t) \left( \int_0^L \rho A x^2 dx + \int_0^L \rho A \left( \sum_{i=1}^{\infty} W_i(x) q_i(t) \right)^2 dx \right) \\
& + \sum_{i=1}^{\infty} \ddot{q}_i(t) \int_0^L \rho A x W_i(x) dx \\
& + 2 \dot{\theta}(t) \int_0^L \rho A \left( \sum_{i=1}^{\infty} W_i(x) q_i(t) \right) \left( \sum_{i=1}^{\infty} W_i(x) \dot{q}_i(t) \right) dx \\
& - g \left( \sin \theta(t) \int_0^L \rho A x dx + \cos \theta(t) \sum_{i=1}^{\infty} q_i(t) \int_0^L \rho A W_i(x) dx \right) = 0
\end{aligned} \tag{2.28}$$

#### 2.4.2: Dynamic simulations

The same simulations are conducted for the linearized and nonlinear systems are conducting here, using the same inputs and physical parameters. The primary difference in the simulation is the introduction of Fourth Order Runge-Kutta approach to give a better estimate of the gradient of the solution over the sampling interval [46]. The Fourth Order Runge-Kutta Scheme is shown in (2.29) – (2.33).

$$c_1 = \dot{X}_k(t, X_k) \tag{2.29}$$

$$c_2 = \dot{X}_k \left( t + \frac{1}{2} dt, X_k + \frac{1}{2} c_1 \right) \tag{2.30}$$

$$c_3 = \dot{X}_k \left( t + \frac{1}{2} dt, X_k + \frac{1}{2} c_2 \right) \quad (2.31)$$

$$c_4 = \dot{X}_k(t + dt, X_k + c_3) \quad (2.32)$$

$$X_{k+1} = X_k + \frac{1}{6} dt(c_1 + 2c_2 + 2c_3 + c_4) \quad (2.33)$$

Here,  $dt = 10^{-3}$  seconds. This method was not used in prior calculations due to the effect of the added complexity on the simulation time.

The results are shown in Figures 2.9-2.12

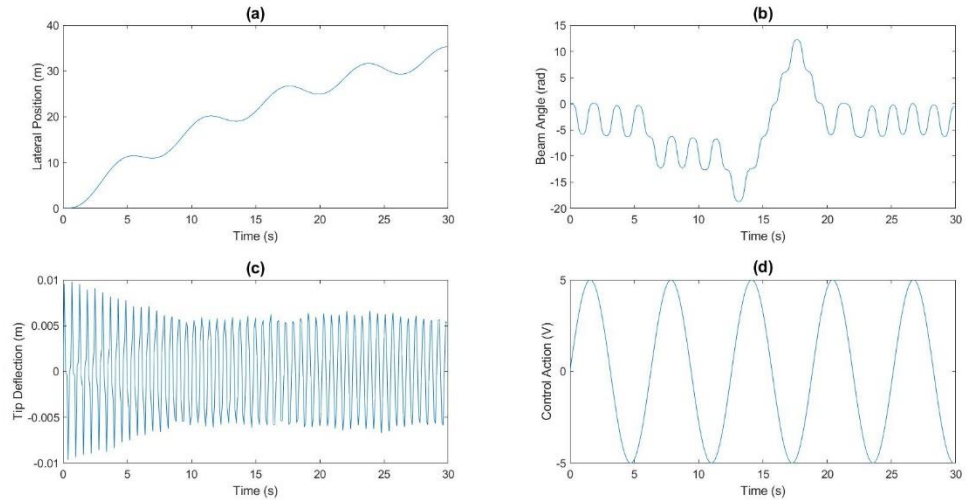


Figure 2.9: (a) Lateral Position, (b) Beam Angle, (c) Tip Deflection, and (d) Control Action Response of System to Sinusoidal Input  $V(t) = 5 \sin t$  volts

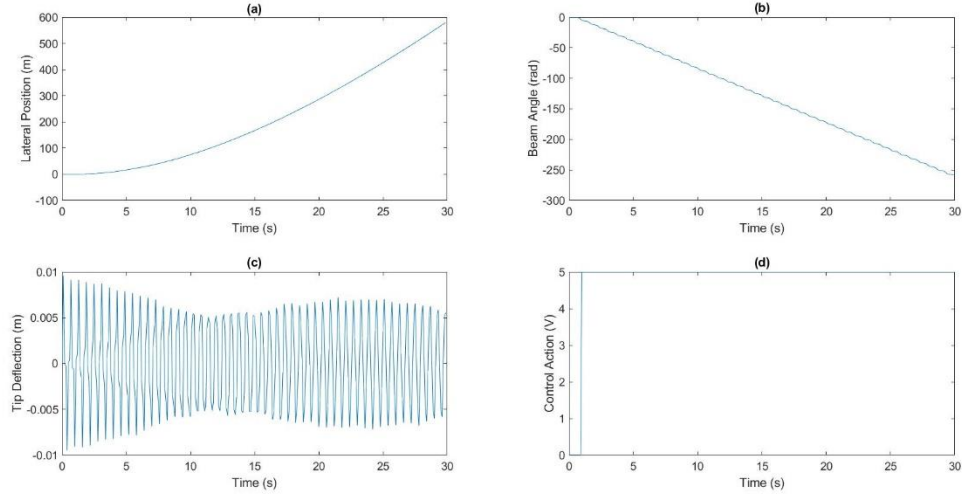


Figure 2.10: (a) Lateral Position, (b) Beam Angle, (c) Tip Deflection, and (d) Control Action Response of System to step input  $V(t) = 5$  volts at  $t = 1$  second

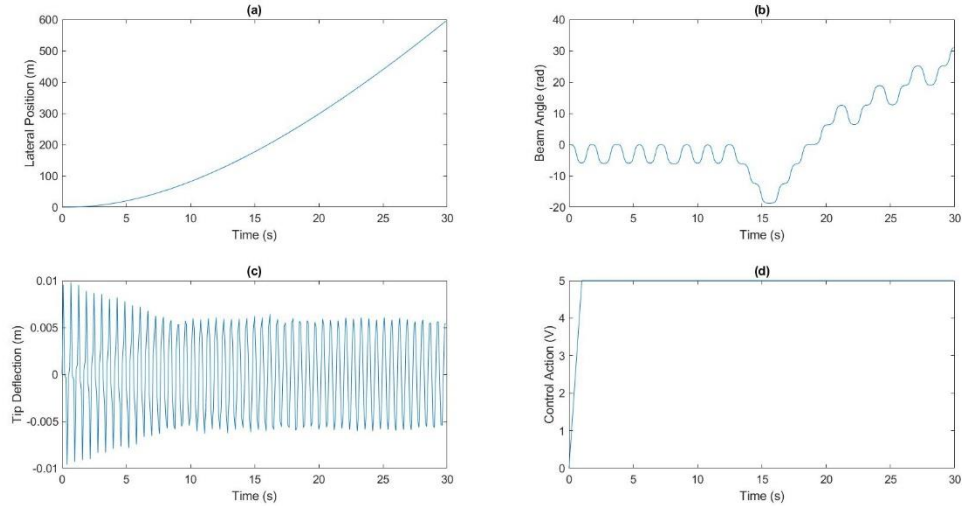


Figure 2.11: (a) Lateral Position, (b) Beam Angle, (c) Tip Deflection, and (d) Control Action Response of System to Ramp Input  $V = 5t$  volts

## Chapter 3: Control via MPC

This chapter will discuss the design and simulation of MPCs for the different model approximations presented in Chapter 2. Because of the difference in models, new controllers needed to be developed for each model, with each controller having different specifications and complexities. This chapter will discuss controller design, including cost functions, weight and constraint selection, controller implementation using MATLAB, and simulation results. Several features of the MPCs were dictated by the physical parameters of the system. These included the limits of the control action  $u$ , which were set to  $\pm 5V$ , as that is the voltage range the DC motor being used is capable of. The limits of the lateral displacement  $x_c(t)$  were also set at  $\pm 1m$ . These limits were applied to all controllers described in this chapter.

### 3.1 Optimization Problem

A major aspect of MPCs is the solving of the optimization problem to determine the optimal set of control actions over the given control horizon based on a given cost function. For the controllers presented here, the same cost function is used for each, shown in (3.1)

$$J(z_k) = J_y(z_k) + J_{\Delta u}(z_k) + J_e(z_k) \quad (3.1)$$

Where  $z_k$  is the set of calculated control action over the prediction horizon,  $k$  is the current control interval, and each  $J$  term is a different function, each focusing on a given aspect of the control performance [47].

The first term,  $J_y(z_k)$ , is given by (3.2), and is the term that tracks the output reference, and calculates the cost of all the error of the output variables and the reference trajectories.

$$J_y(z_k) = \sum_{j=1}^{n_y} \sum_{i=1}^p \left\{ \frac{w_{i,j}^y}{s_j^y} [r_j(k+i) - y_j(k+i)] \right\}^2 \quad (3.2)$$

Where  $p$  is the prediction horizon,  $n_y$  is the number of output variables,  $y_j(k+i)$  is the predicted value of the  $j^{th}$  output variable at the  $i^{th}$  control interval,  $r_j(k+i)$  is the reference trajectory of the  $j^{th}$  output variable at the  $i^{th}$  control interval,  $w_{i,j}^y$  is the weight of the  $j^{th}$  output variable at the  $i^{th}$  control interval, and  $s_j^y$  is the scale factor of the  $j^{th}$  output variable.  $p, n_y, w_{i,j}^y$ , and  $s_j^y$  are constant controller specifications.

The second term,  $J_{\Delta u}(z_k)$ , is given by (3.3), and is the term that tracks the change in the control action between intervals (moves), and calculates the cost of this change.

$$J_{\Delta u}(z_k) = \sum_{j=1}^{n_u} \sum_{i=0}^{p-1} \left\{ \frac{w_{i,j}^{\Delta u}}{s_j^u} [u_j(k+i) - u_j(k+i-1)] \right\}^2 \quad (3.3)$$

Where  $n_u$  is the number of input variables,  $u_j(k+i)$  is the predicted value of the  $j^{th}$  output variable at the  $i^{th}$  control interval,  $w_{i,j}^{\Delta u}$  is the weight of the  $j^{th}$  input move at the  $i^{th}$  control interval, and  $s_j^u$  is the scale factor of the  $j^{th}$  input variable.  $n_u$ ,  $w_{i,j}^{\Delta u}$ , and  $s_j^u$  are constant controller specifications. The controller also applies a constraint when  $i > m$ , where  $m$  is the control horizon, such that  $u_j(k+i) - u_j(k+i-1) = 0$  for  $i > m$ .

The third term,  $J_\epsilon$ , is the term associated with the violation of the given MPC constraints. In order for the given problem to be feasible, some MPC constraints may be violated while solving the problem. Constraints that are allowed to be violated are known as “soft constraints”, and constraints that prohibit violation are known as “hard constraints”. For soft constraints,  $J_\epsilon$  calculates the cost of violating the constraints, and is given by (3.4)

$$J_\epsilon = \rho_\epsilon \epsilon_k^2 \quad (3.4)$$

Where  $\rho_\epsilon$  is the constraint violation penalty weight, and  $\epsilon_k$  is the slack variable at control interval  $k$ ; a higher value of  $\epsilon_k$  indicates a softer constraint, while a value of  $\epsilon_k = 0$  indicates a hard constraint.

The controller solves (3.1) iteratively to minimize the total cost over the prediction horizon in order to find the optimal set of future control actions  $z_k$  over the control horizon.

### 3.2 Linearized Lumped-Parameter System

The first system considered is the linearized lumped-parameter model presented in section 2.2.

#### 3.2.1 Control Design

Since this model is linear, a linear MPC can be used. This control scheme closely mimics that of an LQR, with the main difference being the constraints applied to the controller. The state-space representation of the model equations in (2.7) and (2.8) can be shown in (3.6).

$$\begin{bmatrix} \dot{x}_c \\ \ddot{x}_c \\ \dot{\theta} \\ \ddot{\theta} \end{bmatrix} = \frac{1}{3M_w} \begin{bmatrix} 0 & 3M_w & 0 & 0 \\ 0 & -\frac{2K_mK_tK_g^2}{Rr} & Mgr\left(2 + \frac{L^2Mg}{GJ}\right) & -\frac{rc(MgL^2 + 2GJ)}{LGJ} \\ 0 & 0 & 0 & \frac{3M_w}{2} \\ 0 & \frac{4GJK_g^2K_mK_t}{Lrr^2(MgL^2 + 2GJ)} & \frac{2Rgr^2\left(M + \frac{3}{2}M_w\right)}{Lrr^2} & \frac{2c\left(M + \frac{3}{2}M_w\right)}{L^2M} \end{bmatrix} \begin{bmatrix} x_c \\ \dot{x}_c \\ \theta \\ \dot{\theta} \end{bmatrix} \\
y = \begin{bmatrix} 1 & 0 & 0 & 0 \end{bmatrix} \begin{bmatrix} x_c \\ \dot{x}_c \\ \theta \\ \dot{\theta} \end{bmatrix}$$
(3.5)

Here, the outputs are chosen as the lateral position of the system, and the angle of the beam. This results in an MPC with 4 states, 2 output variables, and 1 input variables

Because of the linear nature of the model, (3.1) can be simplified to a general form Quadratic Programming (QP) problem in (3.6) [33].

$$\begin{aligned}
& \frac{1}{2} z_k^T H z_k + f^T z_k \\
& \text{subject to linear inequality} \\
& A z_k < b
\end{aligned}$$
(3.6)

(3.6) is solved using the KWIK algorithm described in [48]. Since (3.5) requires all states to calculate the optimal cost, an observer is included in the control scheme in the form of a Kalman filter to estimate the unmeasured states [49].

For the linear controller, the control parameters in Table 3.1 were used

Table 3.1: MPC Parameters for Linear System

Parameter	Symbol	Value	Unit
Prediction Horizon	$p$	10	Seconds
Control Horizon	$m$	5	Seconds
Sampling Rate	$T_s$	10	Hz
Output Weights	$w_j^y$	[1 0.9]	-
Input Weights	$w_j^u$	1	-
Output Scale Factors	$s_j^y$	[1 1]	-
Input Scale Factors	$s_j^u$	1	-

### 3.2.2 Control Simulation

The closed-loop system was simulated in response to an output reference trajectory  $r_j = \begin{bmatrix} 1/3 \\ 0 \end{bmatrix}$  applied at  $t = 1$  second, with simulated sensor noise on the order of  $10^{-3}$  applied to both outputs. The results of the simulation are shown below in Figure 3.1

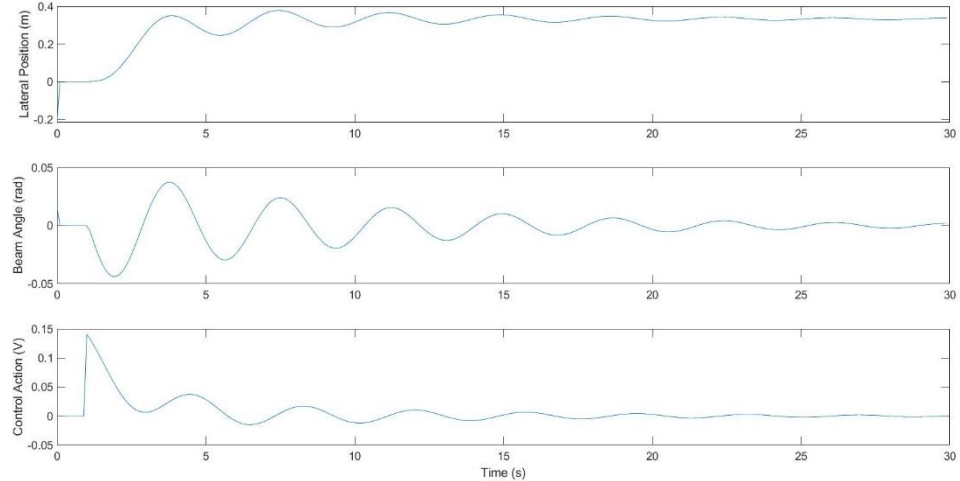


Figure 3.1: Lateral Position (top), Beam Angle (middle), and Control Action (bottom) for Simulated Linear MPC

### 3.3 Nonlinear Lumped-Parameter System

The second system considered is the nonlinear lumped-parameter system presented in Chapter 2.3

### 3.3.1 Control Design

This controller is designed in a similar way to the linear controller, using the same controller parameters given in Table 3.1, with the only difference being the model used.

Since the system is nonlinear, we can no longer represent the system by the state space representation given in (3.5). Rather, the system must be represented by (3.7)

$$\begin{bmatrix} \dot{x}_c \\ \ddot{x}_c \\ \dot{\theta} \\ \ddot{\theta} \end{bmatrix} = f(x_c, \dot{x}_c, \theta, \dot{\theta})$$

$$y = \begin{bmatrix} 1 & 0 & 0 & 0 \\ 0 & 0 & 1 & 0 \end{bmatrix} \begin{bmatrix} x_c \\ \dot{x}_c \\ \theta \\ \dot{\theta} \end{bmatrix} \quad (3.7)$$

Where  $f(x_c, \dot{x}_c, \theta, \dot{\theta})$  is the vector of equations given by (2.10) – (2.11).

### 3.3.2 Control Simulation

The closed-loop system was simulated under the same conditions as the simulation in section 3.2.2. The results of this simulation are shown in Figure 3.2

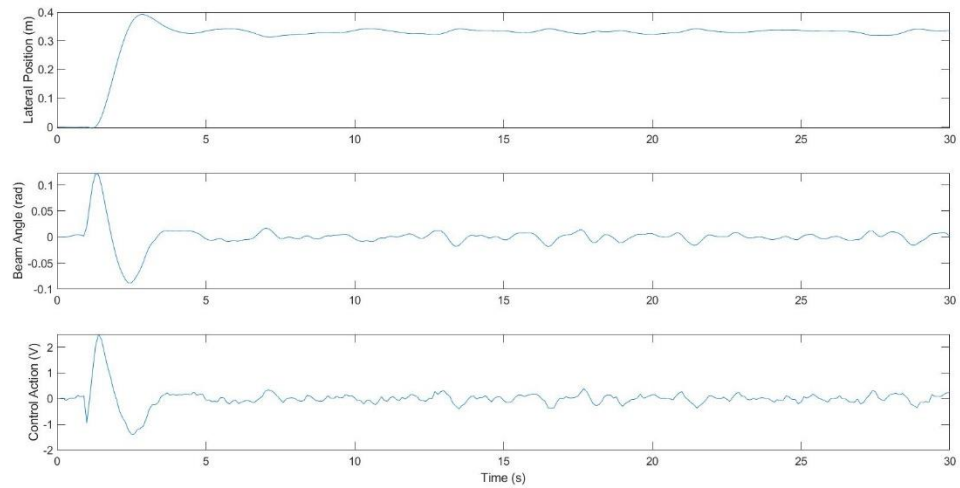


Figure 3.2: Lateral Position (top), Beam Angle (middle), and Control Action (bottom) for Simulated Nonlinear MPC

This controller has a noisier signal than the linear controller, but has better settling time and overall performance.

### 3.4 Continuous system

The final system considered is the fully continuous beam system. This system introduces the deflection of the tip as a point of consideration, increasing the complexity of the controller.

#### 3.4.1 Control Design

For this controller, the system states were adjusted to include the tip deflection as a state of the system. This adjustment is shown in (3.8)

$$\begin{aligned} \begin{bmatrix} \dot{x}_c \\ \ddot{x}_c \\ \dot{\theta} \\ \ddot{\theta} \\ \dot{q}_1 \\ \ddot{q}_1 \\ \vdots \\ \dot{q}_n \\ \ddot{q}_n \end{bmatrix} &= f(x_c, \dot{x}_c, \theta, \dot{\theta}, q_1, \dot{q}_1, \dots, q_n, \dot{q}_n) \\ y = \begin{bmatrix} 1 & 0 & 0 & 0 & 0 & 0 & \cdots & 0 & 0 \\ 0 & 0 & 1 & 0 & 0 & 0 & \cdots & 0 & 0 \\ 0 & 0 & 0 & 0 & W_1(L) & 0 & \cdots & W_n(L) & 0 \end{bmatrix} \begin{bmatrix} x_c \\ \dot{x}_c \\ \theta \\ \dot{\theta} \\ q_1 \\ \dot{q}_1 \\ \vdots \\ q_n \\ \dot{q}_n \end{bmatrix} \end{aligned} \quad (3.8)$$

Where  $f(x_c, \dot{x}_c, \theta, \dot{\theta}, q_1, \dot{q}_1, \dots, q_n, \dot{q}_n)$  is the vector of equations given by (2.12) – (2.14).

The outputs for this system are the system lateral position and beam angle, as before, and the deflection of the tip of the beam. This is a weighted sum of the all the modal  $q_n$  terms, each weighted by the spatial-dependent portion  $W_n(x)$  of the partial differential equation at  $x = L$  that represents the deflection at the beam tip,  $w(L, t)$ . Here,  $n = 2$  vibrational modes are considered, reducing (3.8) to (3.9).

$$\begin{bmatrix} \dot{x}_c \\ \ddot{x}_c \\ \dot{\theta} \\ \ddot{\theta} \\ \dot{q}_1 \\ \ddot{q}_1 \\ \dot{q}_2 \\ \ddot{q}_2 \end{bmatrix} = f(x_c, \dot{x}_c, \theta, \dot{\theta}, q_1, \dot{q}_1, q_2, \dot{q}_2) \quad (3.9)$$

$$y = \begin{bmatrix} 1 & 0 & 0 & 0 & 0 & 0 & 0 & 0 \\ 0 & 0 & 1 & 0 & 0 & 0 & 0 & 0 \\ 0 & 0 & 0 & 0 & W_1(L) & 0 & W_2(L) & 0 \end{bmatrix} \begin{bmatrix} x_c \\ \dot{x}_c \\ \theta \\ \dot{\theta} \\ q_1 \\ \dot{q}_1 \\ q_2 \\ \dot{q}_2 \end{bmatrix}$$

This configuration results in an MPC with 8 states, 3 outputs, and 1 manipulated input. The control parameters used are shown in Table 3.2

Table 3.2: MPC Parameters for Continuous System

Parameter	Symbol	Value	Unit
Prediction Horizon	$p$	10	Seconds
Control Horizon	$m$	5	Seconds
Sampling Rate	$T_s$	10	Hz
Output Weights	$w_j^y$	[1 2 1]	-
Input Weights	$w_j^u$	1	-
Output Scale Factors	$s_j^y$	[1 1 1]	-
Input Scale Factors	$s_j^u$	1	-

Additionally, the piezoelectric actuator at the base of the beam was given a voltage input of  $v = \sin(3.3\pi t)V$ . This excites the beam, creating vibration at the tip to simulate an operator, which the controller will be tasked with minimizing.

### 3.4.2 Controller Simulation

The closed-loop system was simulated in response to an output reference trajectory  $r_j = \begin{bmatrix} 1/3 \\ 0 \\ 0 \end{bmatrix}$

applied at  $t = 1$  second, with simulated sensor noise on the order of  $10^{-3}$  applied to both outputs.

The results of the simulation are shown below in Figures 3.3.

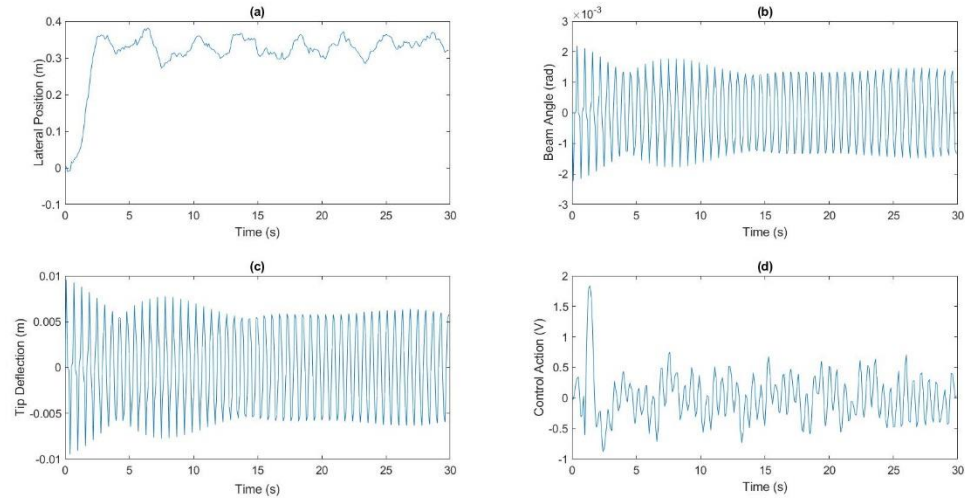


Figure 3.3: Lateral Position (a), Beam Angle (b), Tip Deflection (c), and Control Action (d) of Continuous Beam System Closed-Loop Response with MPC

These figures show that the MPC of the continuous system is able to maintain the stability of the system and keep the beam vertical, even when the beam is excited by the piezoelectric actuator.

## Chapter 4: Model Mismatch and Controller Comparison

This chapter will investigate the effectiveness of different controllers paired with different models. The goal of this is to determine the minimum complexity the controller model needs to have to control a given system, meaning, could the linear controller control the nonlinear system? Or the nonlinear controller control the continuous system? Since MPCs have a high computational load, minimizing the amount of on-line computation necessary for a given system would improve the efficiency of the entire setup. This chapter will investigate the ability of the linear controller to control the nonlinear system, and both the linear and nonlinear controllers to control the continuous system.

### 4.1 Linear controller for nonlinear system

Here, the linear MPC will be used in conjuncture with the nonlinear model. The same system and simulation parameters from section 3.2 are used. The simulation results are shown below in Figure 4.1

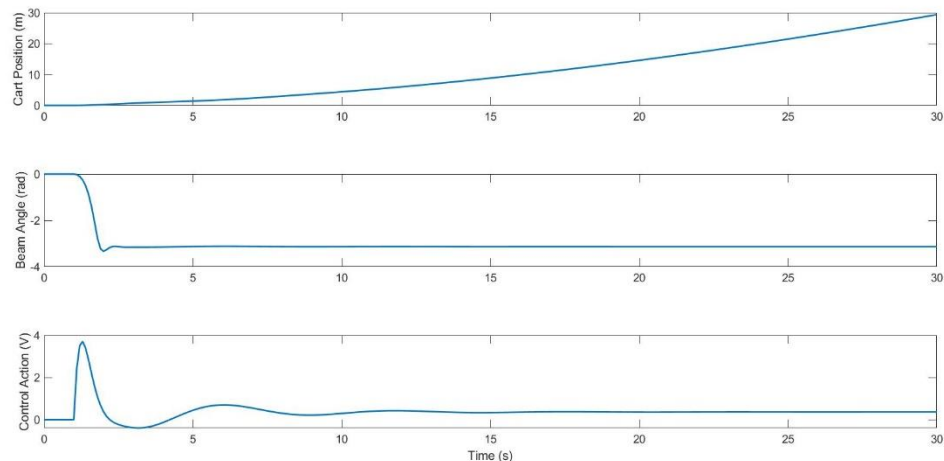


Figure 4.1: Lateral Position (top), Beam Angle (middle), and Control Action (bottom) for the Nonlinear System with a Linear Controller

From Figure 4.2, it is shown that the linear controller is not capable of controlling the nonlinear system. The beam very quickly loses stability when the reference trajectory signal is applied.

## 4.2 Linear Controller for Continuous System

Here, the linear MPC will be used in conjuncture with the continuous model. The same system and simulation parameters from section 3.2 are used. Since the linear controller only has 4 states and 2 outputs, the tip deflection was ignored by the MPC algorithm. The simulation results are shown below in Figure 4.2

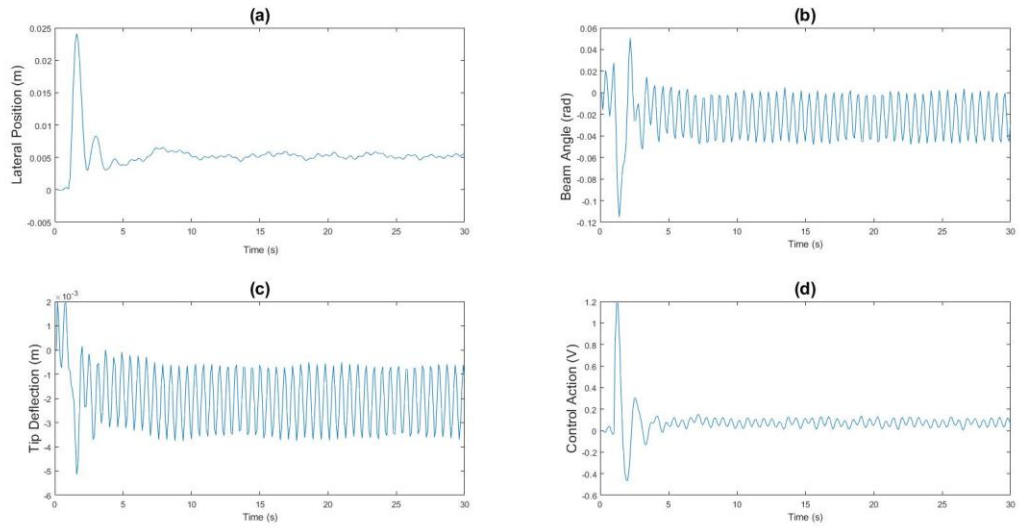


Figure 4.2: Lateral Position (a), Beam Angle (b), Tip Deflection (c), and Control Action (d) for the Continuous System with a Linear Controller

From Figure 4.2, it is shown that the linear controller is not capable of controlling the continuous system. While it does appear to maintain stability, it never actually translates the system to the desired setpoint, and has unrealistic results for the beam angle and tip deflection, as they oscillate about points other than their equilibrium.

## 4.3 Nonlinear Controller for Continuous System

Here, the nonlinear MPC will be used in conjuncture with the continuous model. The same system and simulation parameters from section 3.2 are used, except the motor voltage limit was increased to  $\pm 12V$ . Since the nonlinear controller only has 4 states and 2 outputs, the tip deflection was ignored by the MPC algorithm. The results are shown below in Figure 4.3

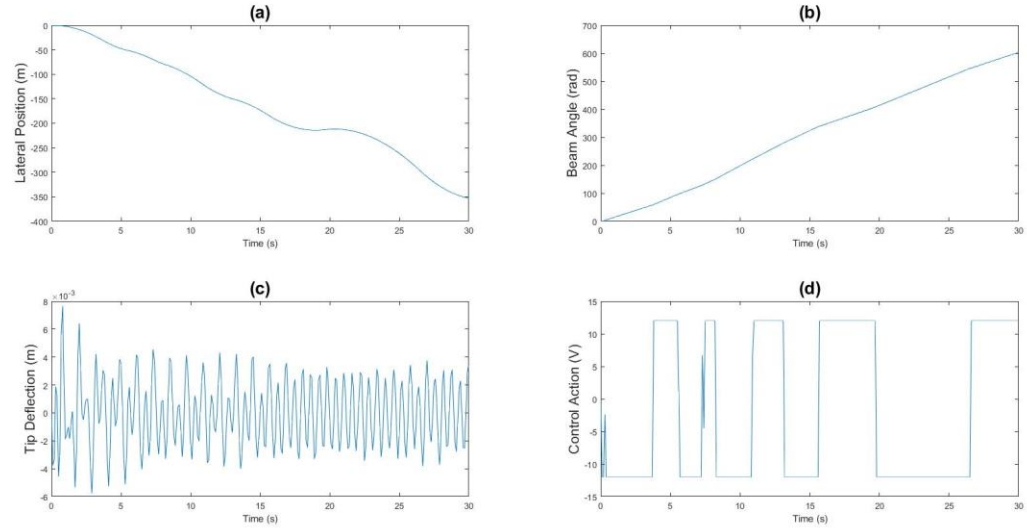


Figure 4.3: Lateral Position (a), Beam Angle (b), Tip Deflection (c), and Control Action (d) for the Continuous System with a Nonlinear Controller

From Figure 4.3, it is shown that the nonlinear controller is not capable of controlling the continuous system. The beam angle never becomes stable, and the motor voltage frequently becomes saturated.

## Chapter 5: Conclusions and Future Work

### 5.1 Conclusions

From the controller simulation results in Chapter 3, it is shown that the designed controller is capable of maintaining stability of the beam-hoverboard system model, keeping the angle of the beam base  $< |2.5 \times 10^{-3}| \text{ rad}$ , and controlling the deflections in the tip of the beam to a reasonable degree,  $< |0.01| \text{ m}$ . This shows the feasibility of using MPC to control extremely complex continuous systems. While this controller proved successful in meeting performance requirements, it is an impractical controller, due mostly to its inefficiency; the simulation shown in Figure 3.3 took nearly 12 full hours to run. This can be attributed mostly to the optimization algorithm, as it needed to numerically iterate through sets of future control inputs to find the optimal solution to (3.1). This sort of run time would prove difficult in an experimental system, where on-line calculations would need to be done in real-time. This is why it was desired to find a simplified controller that would be able to meet the desired performance specifications for the continuous system.

However, developing a simplified controller to control the continuous system proved unsuccessful, as only the controller developed using fully continuous model was able to meet the desired performance specifications, as shown in Chapter 4. This result is not that surprising, as MPCs lack robustness when dealing with model uncertainty [40]. There are several techniques for analyzing MPC robustness, but very few for robust MPC synthesis [43], and most deal with uncertainty within the system parameters, not a model mismatch, as was applied here.

### 5.2 Future Work

This section will introduce future work, including improvements to the controller algorithm, proposed experimental designs, and further modelling of more complex systems.

#### 5.2.1 Explicit MPC

One of the major disadvantages of MPC is the inefficiency related to the on-line computation related to the optimization problem. In this case, simulation time of +12 hours were necessary to solve the optimization problem for 30 seconds worth of control actions. This is not feasible in experimentation, as the system is desired to be at an unstable equilibrium, and would not take long to lose its equilibrium if disturbed.

An approach to remedy this is to develop an Explicit MPC, which exploits multiparametric programming techniques to compute the optimal control actions as an “explicit” function for a given range of operating conditions off-line [50]. This reduces the on-line computations to a lookup table of linear gains, greatly decreasing the on-line computational load. Since the proposed system here operates within a known range of operating conditions (voltage input, beam angle, etc...), an Explicit MPC could be developed to reduce online computations and make the controller efficient enough to be used with an experimental system.

### 5.2.2 Experimental Setup

To experimentally validate the developed controller, the following experimental apparatus is proposed. This system is essentially a belt-driven gantry, with a flexible beam mounted to it to mimic the system proposed in section 2.1. A 12V DC motor is used to power the system, with optical encoders at both the motor shaft and beam base to measure lateral position and beam rotation, respectively. As with the system proposed in section 2.1, a piezoelectric actuator is mounted to the beam base, acting as both an actuator and a sensor to measure the deflection of the beam. This proposed experimental system is shown in Figure 5.1.



Figure 5.1: CAD Model of Proposed Experimental Setup (belt and motor not shown)

In order to confirm the validity of this proposed system, the controller designed in section 3.4.1 was used with the physical parameters Table 5.1. Since this system uses several stationary and nonuniform rotating and translating components, it's physical parameters must be expressed in terms of the mass of the translating components and the inertia and radii of the rotating components.

Table 5.1: Physical Parameters of Proposed Experimental Setup

Parameter	Symbol	Value	Unit
Mass of the Translating Bodies	$M$	0.024	kg
Inertias of the Rotating Bodies	$I_w$	$[0.0038 \quad 3.5117 \cdot 10^{-5}]$	$\text{kg}^*\text{m}^2$
Length of the beam	$L$	0.18	m
Radius of the Wheels	$r$	$[0.0119 \quad 0.0142]$	m
Internal gear ratio	$K_g$	4.385: 1	-
Motor torque constant	$K_t$	0.00767	Nm/Amp
Motor Armature Resistance	$R$	2.6	$\Omega$
Gravitational constant of earth	$g$	9.81	$\text{m/s}^2$
Elastic Modulus of Beam	$G$	70	GPa
Second moment of Area of Beam	$J$	$8.335 * 10 - 7$	$\text{m}^4$

The results of this simulation are shown below in Figure 5.2

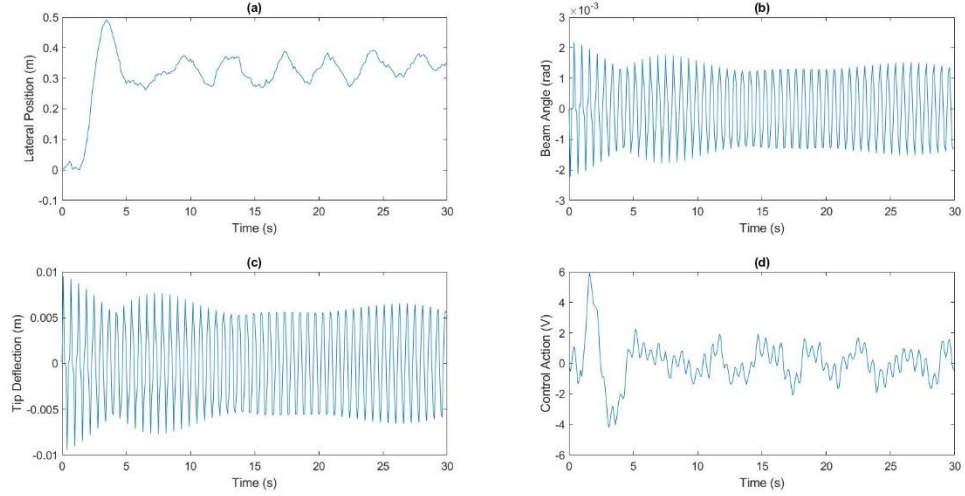


Figure 5.2: Lateral Position (a), Beam Angle (b), Tip Deflection (c), and Control Action (d) for the Proposed Experimental System

Based on these results, it can be seen that the proposed experimental setup can be adequately controlled by using the MPC designed previously.

### 5.2.3 Lumped-Parameter Double-Beam Model

A further model was developed for a more complex system, similar to the lumped-parameter system proposed in section 2.1, shown in Figure 5.3. This system uses two independently rotating platforms to control motion of the system in 2d space. Each platform has an inverted pendulum mounted to it, which rotates in the same manner as the lumped-parameter introduced in section 2.1. Each platform has an independent DC motor connected to a wheel, allowing each wheel to rotate independently to create motion in the XY plane.

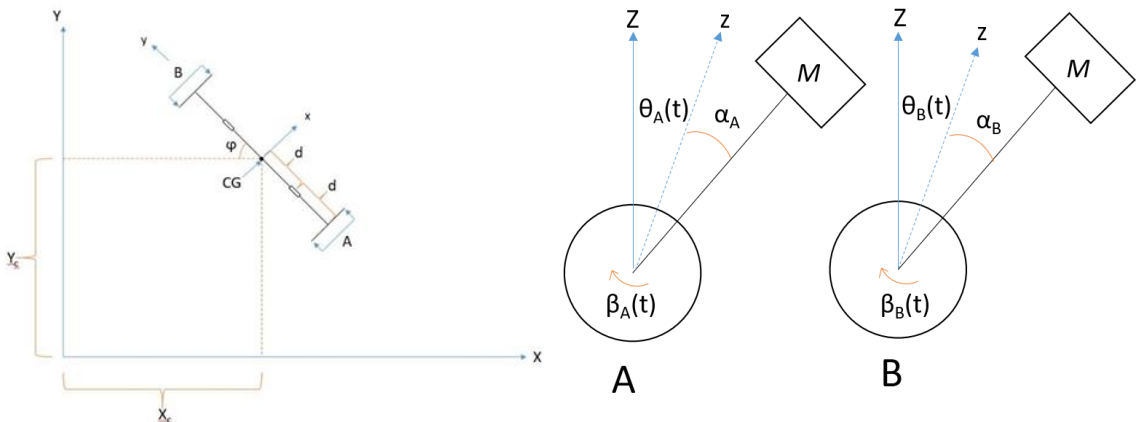


Figure 5.3: XY Plane View of Top (left) and Side (right) View of Double Beam System

Where  $x_c(t)$  and  $y_c(t)$  are the X and Y positions of the center of gravity of the system, respectively,  $d$  is the distance from both the wheel to the beam and the beam to the center of gravity, and  $\varphi$  is the angle the system makes with the X-axis. Additionally,  $\alpha_A(t)$  and  $\alpha_B(t)$  have the same relationship to  $\theta_A(t)$  and  $\theta_B(t)$ , respectively, as  $\alpha(t)$  does to  $\theta(t)$  as described in (2.2). This system has 5 generalized coordinates,  $\{x_c(t), y_c(t), \varphi(t), \theta_A(t), \theta_B(t)\}$

To model this system, the same Lagrangian mechanics used in section 2.1 can be applied. First, the kinetic energy of the system is determined.  $\gamma_A(t)$  and  $\gamma_B(t)$  can be used to temporarily represent  $\theta_A(t) + \alpha_A(t)$  and  $\theta_B(t) + \alpha_B(t)$ , respectively.

$$\begin{aligned} KE = & \frac{M}{2} \left( (\dot{x}_c - L\dot{\varphi} \sin \varphi (\sin \gamma_A + \sin \gamma_B) + L \cos \varphi (\dot{\gamma}_A \cos \gamma_A + \dot{\gamma}_B \cos \gamma_B))^2 \right. \\ & + (\dot{y}_c - L\dot{\varphi} \cos \varphi (\sin \gamma_A + \sin \gamma_B) + L \sin \varphi (\dot{\gamma}_A \cos \gamma_A \\ & \left. + \dot{\gamma}_B \cos \gamma_B))^2 + L^2(\dot{\gamma}_A^2 \sin^2 \gamma_A + \dot{\gamma}_B^2 \sin^2 \gamma_B) \right) \\ & + \frac{3}{2} M_w (\dot{x}_c^2 + \dot{y}_c^2 + 4d^2 \dot{\varphi}^2) \end{aligned} \quad (5.1)$$

The potential energy can also be determined

$$PE = Mg(\cos \gamma_A + \cos \gamma_B) \quad (5.2)$$

This yields a Lagrangian of

$$\begin{aligned} \mathbb{L} = & \frac{M}{2} \left( (\dot{x}_c - L\dot{\varphi} \sin \varphi (\sin \gamma_A + \sin \gamma_B) + L \cos \varphi (\dot{\gamma}_A \cos \gamma_A + \dot{\gamma}_B \cos \gamma_B))^2 \right. \\ & + (\dot{y}_c - L\dot{\varphi} \cos \varphi (\sin \gamma_A + \sin \gamma_B) + L \sin \varphi (\dot{\gamma}_A \cos \gamma_A \\ & \left. + \dot{\gamma}_B \cos \gamma_B))^2 + L^2(\dot{\gamma}_A^2 \sin^2 \gamma_A + \dot{\gamma}_B^2 \sin^2 \gamma_B) \right. \\ & \left. - 2g(\cos \gamma_A + \cos \gamma_B) \right) + \frac{3}{2} M_w (\dot{x}_c^2 + \dot{y}_c^2 + 4d^2 \dot{\varphi}^2) \end{aligned} \quad (5.3)$$

This Lagrangian can be applied to (2.3), along with the set of generalized forces for each of the 5 generalized coordinates shown in (5.4).

$$\begin{bmatrix} \Sigma_{x_c} \\ \Sigma_{y_c} \\ \Sigma_\varphi \\ \Sigma_{\gamma_A} \\ \Sigma_{\gamma_B} \end{bmatrix} = \begin{bmatrix} \sigma_1 \left( \frac{\sigma_4}{\sigma_5} + \frac{\sigma_3}{2r\sigma_6} \right) \\ (2y_c(t) - \sigma_2 + 2L \sin \varphi(t)) \left( \frac{\sigma_4}{\sigma_5} \sin \gamma_A(t) + \frac{\sigma_3}{2r\sigma_6} \sin \gamma_B(t) \right) \\ \frac{\sigma_4}{\sigma_5} (\sigma_7 + 2\sigma_{10}(\sigma_{17} + \sigma_{18})) + \frac{\sigma_3}{2r\sigma_6} (\sigma_7 + 2\sigma_{11}(\sigma_{17} + L \cos \varphi(t) \sin \gamma_B(t))) \\ \frac{\sigma_4}{\sigma_5} (2L \cos \gamma_A(t) (\sigma_{12} \cos \varphi(t) + \sigma_{10} \sin \varphi(t))) + \frac{L\sigma_3\sigma_{12}}{r\sigma_6} \cos \gamma_A(t) \cos \varphi(t) \\ \frac{L\sigma_3\sigma_{11}}{r\sigma_6} \cos \gamma_B(t) \sin \varphi(t) \end{bmatrix} \quad (5.4)$$

Where:

$$\sigma_1 = 2(x_c(t) + d \sin \varphi(t) + L \cos \varphi(t) \sin \gamma_A(t))$$

$$\begin{aligned}
\sigma_2 &= 2d \cos \varphi(t) \\
\sigma_3 &= \frac{K_t K_g}{R} V_B(t) \\
&\quad - \left( \frac{c}{r} + \frac{K_t K_g^2 K_m}{rR} \right) \sqrt{(\dot{y}_c(t) - 2d\dot{\varphi}(t) \cos \varphi(t))^2 + (\dot{x}_c(t) - 2d\dot{\varphi}(t) \sin \varphi(t))^2} \\
\sigma_4 &= \frac{K_t K_g}{R} V_A(t) - \left( \frac{c}{r} + \frac{K_t K_g^2 K_m}{rR} \right) \sqrt{(\dot{y}_c(t) - 2d\dot{\varphi}(t) \cos \varphi(t))^2 + (\dot{x}_c(t) - 2d\dot{\varphi}(t) \sin \varphi(t))^2} \\
\sigma_5 &= 2r \sqrt{(x_c(t) - d \sin \varphi(t) + L \cos \varphi(t) \sin \gamma_A(t))^2 + (y_c(t) - d \cos \varphi(t) + L \sin \gamma_A(t) \sin \varphi(t))^2} \\
\sigma_6 &= \sqrt{(x_c(t) - d \sin \varphi(t) + L \cos \varphi(t) \sin \gamma_A(t))^2 + (y_c(t) - d \cos \varphi(t) + L \sin \gamma_B(t) \sin \varphi(t))^2} \\
\sigma_7 &= 2(d \cos \varphi(t) - L \sin \gamma_A(t) \sin \varphi(t))(x_c(t) - d \sin \varphi(t) + L \cos \varphi(t) \sin \gamma_A(t)) \\
\sigma_8 &= \sqrt{(\dot{y}_c(t) - 2d\dot{\varphi}(t) \cos \varphi(t))^2 + (\dot{x}_c(t) - 2d\dot{\varphi}(t) \sin \varphi(t))^2} \\
\sigma_9 &= \sqrt{(\dot{y}_c(t) - 2d\dot{\varphi}(t) \cos \varphi(t))^2 + (\dot{x}_c(t) - 2d\dot{\varphi}(t) \sin \varphi(t))^2} \\
\sigma_{10} &= y_c(t) - d \cos \varphi(t) + L \sin \gamma_A(t) \sin \varphi(t) \\
\sigma_{11} &= y_c(t) - d \cos \varphi(t) + L \sin \gamma_B(t) \sin \varphi(t) \\
\sigma_{12} &= x_c(t) - d \sin \varphi(t) + L \cos \varphi(t) \sin \gamma_A(t) \\
\sigma_{13} &= 2d\dot{\varphi}(t) \sin \varphi(t) \\
\sigma_{14} &= 2d\dot{\varphi}(t) \cos \varphi(t) \\
\sigma_{15} &= L \sin \gamma_A(t) \sin \varphi(t) \\
\sigma_{16} &= d \cos \varphi(t) \\
\sigma_{17} &= d \sin \varphi(t) \\
\sigma_{18} &= L \cos \varphi(t) \sin \gamma_A(t)
\end{aligned}$$

This yields the equations of motion for the linearized double beam model shown in (5.5) – (5.9)

$$\begin{aligned}
& 3M_w \ddot{x}_c(t) \\
& - ML \left( \cos \varphi(t) (\sin \gamma_B(t) (\dot{\gamma}_B^2(t) + \dot{\varphi}^2(t)) - \cos \gamma_B(t) \dot{\gamma}_B(t) \right. \\
& - \sin \gamma_A(t) (\dot{\gamma}_A^2(t) + \dot{\varphi}^2(t)) + \cos \gamma_A(t) \dot{\gamma}_A(t) \\
& + \sin \varphi(t) (\ddot{\varphi}(t) (\sin \gamma_B(t) - \sin \gamma_A(t)) \\
& \left. + 2\dot{\varphi}(t) (\dot{\gamma}_B(t) \cos \gamma_B(t) - \dot{\gamma}_A(t) \cos \gamma_A(t))) \right) \\
& = \frac{\sigma_1}{2r} \frac{K_g K_t}{R} \left( \frac{V_A(t) - \sqrt{(\dot{y}_c(t) + \sigma_4)^2 + (\dot{x}_c(t) + \sigma_3)^2} \left( \frac{K_g K_m}{R} + \frac{Rc}{r K_g K_t} \right)}{\sqrt{\sigma_2 + (y_c(t) - d \cos \varphi(t) + L \sin \gamma_A(t) \sin \varphi(t))^2}} \right. \\
& \left. + \frac{V_B(t) + \sqrt{(\dot{y}_c(t) - \sigma_4)^2 + (\dot{x}_c(t) - \sigma_3)^2} \left( \frac{K_g K_m}{R} + \frac{Rc}{r K_g K_t} \right)}{\sqrt{\sigma_2 + (y_c(t) - d \cos \varphi(t) + L \sin \gamma_B(t) \sin \varphi(t))^2}} \right)
\end{aligned} \tag{5.5}$$

Where:

$$\begin{aligned}
\sigma_1 &= 2x_c(t) + 2d \sin \varphi(t) + 2L \cos \varphi(t) \sin \gamma_A(t) \\
\sigma_2 &= (x_c(t) + d \sin \varphi(t) + L \cos \varphi(t) \sin \gamma_A(t))^2 \\
\sigma_3 &= 2d \dot{\varphi}(t) \sin \varphi(t) \\
\sigma_4 &= 2d \dot{\varphi}(t) \cos \varphi(t)
\end{aligned}$$

$$\begin{aligned}
& \frac{M}{2} \left( 4\ddot{y}_c(t) \right. \\
& - 2L \left( \sin \varphi(t) (\sin \gamma_A(t) (\dot{\gamma}_A^2(t) - \dot{\varphi}^2(t)) + \dot{\gamma}_A(t) \cos \gamma_A(t) - \sin \gamma_B(t) (\dot{\gamma}_B^2(t) - \dot{\varphi}^2(t)) \right. \\
& \left. - \dot{\gamma}_B(t) \cos \gamma_B(t)) \right. \\
& \left. + \cos \varphi(t) (\ddot{\varphi}(t) (\sin \gamma_A(t) - \sin \gamma_B(t)) + 2\dot{\varphi}(t) (\dot{\gamma}_A(t) \cos \gamma_A(t) - \dot{\gamma}_B(t) \cos \gamma_B(t))) \right) \\
& + 3M_w \ddot{y}_c(t) \\
& = \frac{K_g K_t}{R} \left( \frac{(2y_c(t) - 2d \cos \varphi(t) + 2L \sin \gamma_A(t) \sin \varphi(t)) \left( V_A(t) - \sigma_3 \left( \frac{K_g K_m}{Rr} + \frac{Rc}{r K_g K_t} \right) \right)}{2r \sqrt{\sigma_1 + (y_c(t) - d \cos \varphi(t) + L \sin \gamma_A(t) \sin \varphi(t))^2}} \right. \\
& \left. + \frac{(2y_c(t) - 2d \cos \varphi(t) + 2L \sin \gamma_B(t) \sin \varphi(t)) \left( V_B(t) - \sigma_2 \left( \frac{K_g K_m}{Rr} + \frac{Rc}{r K_g K_t} \right) \right)}{2r \sqrt{\sigma_1 + (y_c(t) - d \cos \varphi(t) + L \sin \gamma_B(t) \sin \varphi(t))^2}} \right)
\end{aligned} \tag{5.6}$$

Where:

$$\begin{aligned}
\sigma_1 &= (x_c(t) + d \sin \varphi(t) + L \cos \varphi(t) \sin \gamma_A(t))^2 \\
\sigma_2 &= \sqrt{(\dot{y}_c(t) - 2d \dot{\varphi}(t) \cos \varphi(t))^2 + (\dot{x}_c(t) - 2d \dot{\varphi}(t) \sin \varphi(t))^2} \\
\sigma_3 &= \sqrt{(\dot{y}_c(t) + 2d \dot{\varphi}(t) \cos \varphi(t))^2 + (\dot{x}_c(t) + 2d \dot{\varphi}(t) \sin \varphi(t))^2}
\end{aligned}$$

$$\begin{aligned}
& \frac{K_g K_t}{R} \frac{\left( \frac{\sigma_2}{r} \left( \frac{Rc}{K_g K_t} + K_g K_m \right) - V_A(t) \right)}{\sqrt{\sigma_4^2 + (y_c(t) - d \cos \varphi(t) + L \sin \varphi(t) \sin \gamma_A(t))^2}} \left( 2d(y_c(t) \sin \varphi(t) \right. \\
& \quad \left. + x_c(t) \cos \varphi(t)) + 2L \cos \varphi(t) \sin \gamma_A(t) (y_c(t) - x_c(t)) \right) \\
& \quad + \frac{K_g K_t}{R} \frac{\left( \frac{\sigma_1}{r} \left( \frac{Rc}{K_g K_t} + K_g K_m \right) - V_B(t) \right)}{\sqrt{\sigma_4^2 + \sigma_3^2}} \left( 2(d \cos \varphi(t) \right. \\
& \quad \left. - L \sin \varphi(t) \sin \gamma_A(t)) \sigma_8 + 2\sigma_7 (d \sin \varphi(t) + L \cos \varphi(t) \sin \gamma_B(t)) \right) \quad (5.7) \\
& \quad + 4d^2 r \ddot{\varphi}(t) (M + 6M_w) \\
& \quad + 2LMr \left( 2L\ddot{\varphi}(t) + d\dot{\gamma}_B^2(t) \sin \gamma_B(t) + d\ddot{\gamma}_A(t) \right. \\
& \quad \left. + \dot{y}_c(t) \cos \varphi(t) (\sin \gamma_A(t) + \sin \gamma_B(t)) \right) \\
& \quad + L^2 Mr \dot{\varphi}(t) (\dot{\gamma}_A(t) \sin 2\gamma_A(t) + \dot{\gamma}_B(t) \sin 2\gamma_B(t)) \\
& = 2LMr (\ddot{\varphi}(t) (\cos^2 \gamma_A(t) + \cos^2 \gamma_B(t)) + d\dot{\gamma}_A^2(t) \sin \gamma_A(t) \\
& \quad + d\dot{\gamma}_B^2(t) \cos \gamma_B(t) + \ddot{x}_c(t) \sin \varphi(t) (\sin \gamma_A(t) + \sin \gamma_B(t)))
\end{aligned}$$

Where:

$$\begin{aligned}
\sigma_1 &= \sqrt{(\dot{y}_c(t) - 2d\dot{\varphi}(t) \cos \varphi(t))^2 + (\dot{x}_c(t) - 2d\dot{\varphi}(t) \sin \varphi(t))^2} \\
\sigma_2 &= \sqrt{(\dot{y}_c(t) + 2d\dot{\varphi}(t) \cos \varphi(t))^2 + (\dot{x}_c(t) + 2d\dot{\varphi}(t) \sin \varphi(t))^2} \\
\sigma_3 &= y_c(t) - d \cos \varphi(t) + L \sin \gamma_B(t) \sin \varphi(t) \\
\sigma_4 &= x_c(t) - d \sin \varphi(t) + L \sin \gamma_A(t) \sin \varphi(t)
\end{aligned}$$

$$\begin{aligned}
& LM r \left( 2\ddot{\gamma}_A(t) - L\dot{\varphi}^2(t) \sin 2\gamma_A(t) \right. \\
& \quad \left. + 2 \cos \gamma_A(t) (\ddot{x}_c(t) \cos \varphi(t) + \dot{y}_c(t) \sin \varphi(t) + d\ddot{\varphi}(t)) \right) \\
& = 2LMgr \sin \gamma_A(t) \\
& \quad - 2 \cos \gamma_A(t) \frac{K_g K_t}{R} \left( \frac{\frac{\sigma_4}{r} \left( \frac{cR}{K_g K_t} + K_g K_m \right) - V_A(t)}{\sqrt{\sigma_1^2 + (y_c(t) - \sigma_2 + L \sin \gamma_A \sin \varphi(t))^2}} (x_c(t) \cos \varphi(t) \right. \\
& \quad \left. + y_c(t) \sin \varphi(t) + L \sin \gamma_A(t)) \right. \\
& \quad \left. + \sigma_1 \cos \varphi(t) \frac{\frac{\sigma_3}{r} \left( \frac{cR}{K_g K_t} + K_g K_m \right) - V_B(t)}{\sqrt{\sigma_1^2 + (y_c(t) - \sigma_2 + L \sin \gamma_B \sin \varphi(t))^2}} \right) \quad (5.8)
\end{aligned}$$

Where:

$$\begin{aligned}
\sigma_1 &= x_c(t) + d \sin \varphi(t) + L \cos \varphi(t) \sin \gamma_A(t) \\
\sigma_2 &= d \cos \varphi(t) \\
\sigma_3 &= \sqrt{(\dot{y}_c(t) - 2d\dot{\varphi}(t) \cos \varphi(t))^2 + (\dot{x}_c(t) - 2d\dot{\varphi}(t) \sin \varphi(t))^2} \\
\sigma_4 &= \sqrt{(\dot{y}_c(t) + 2d\dot{\varphi}(t) \cos \varphi(t))^2 + (\dot{x}_c(t) + 2d\dot{\varphi}(t) \sin \varphi(t))^2}
\end{aligned}$$

$$\begin{aligned}
& g \sin \gamma_B(t) + L \cos \gamma_B(t) \sin \gamma_B(t) \dot{\varphi}^2(t) + \dot{y}_c(t) \dot{\varphi}(t) \cos \gamma_B(t) \cos \varphi(t) \\
& - \cos \varphi(t) \sin \gamma_B(t) \dot{y}_B \dot{x}_c(t) - \cos \gamma_B(t) \sin \varphi(t) \dot{\varphi}(t) \dot{x}_c(t) \\
& - \sin \gamma_B(t) \sin \varphi(t) \dot{y}_B(t) \dot{y}_c(t) + d \sin \gamma_B(t) \dot{y}_B(t) \dot{\varphi}(t) \\
& = L \ddot{y}_B(t) + \ddot{x}_c(t) \cos \gamma_B(t) \cos \varphi(t) + \ddot{y}_c(t) \cos \gamma_B(t) \sin \varphi(t) - d \ddot{\varphi}(t) \cos \gamma_B(t) \\
& + \cos \gamma_B(t) \cos \varphi(t) \dot{y}_c(t) \dot{\varphi}(t) - \cos \varphi(t) \sin \gamma_B(t) \dot{y}_B(t) \dot{x}_c(t) \\
& - \cos \gamma_B(t) \sin \varphi(t) \dot{x}_c(t) \dot{\varphi}(t) - \sin \varphi(t) \sin \gamma_B(t) \dot{y}_B(t) \dot{y}_c(t) \\
& + d \sin \gamma_B(t) \dot{y}_B(t) \dot{\varphi}(t) \\
& + 2L\sigma_2 \cos \gamma_B(t) \sin \varphi(t) \frac{K_g K_t}{R} \frac{\left( \frac{\sigma_1}{r} \left( \frac{cR}{K_g K_t} + K_g K_m \right) - V_B(t) \right)}{\sqrt{(x_c(t) + d \sin \varphi(t) + L \cos \varphi(t) \sin \gamma_A(t))^2 + \sigma_2^2}}
\end{aligned} \tag{5.9}$$

Where:

$$\sigma_1 = \sqrt{(\dot{y}_c(t) - 2d\dot{\varphi}(t) \cos \varphi(t))^2 + (\dot{x}_c(t) - 2d\dot{\varphi}(t) \sin \varphi(t))^2}$$

$$\sigma_2 = y_c(t) + d \cos \varphi(t) + L \sin \varphi(t) \sin \gamma_B(t)$$

## REFERENCES

- [1] A. Castro, W. Singhouse, X. Liu, K. Sorensen, and E. C. Kwak, "MODELING AND EXPERIMENTAL TESTING OF HOVERBOARD DYNAMIC BEHAVIOR," in Proc. ASME Dynamic Systems and Control Conference, Tysons, Virginia, USA, 2017: ASME
- [2] W. Masayoshi, "Research and development of electric vehicles for clean transportation," *Journal of Environmental Sciences*, vol. 21, no. 6, pp. 745-749, 2009.
- [3] K. T. Ulrich, "Estimating the technology frontier for personal electric vehicles," *Transportation Research*, vol. 13, no. 5-6, C, pp. 448-462, 2005.
- [4] Somenahalli, Sekhar, Yoshitsugu, Hayashi, Taylor, Michael, Akiyama, Tetsuo, Adair, Timothy, Sawada, Daisuke. "Accessible transportation and mobility issues of elderly — how does Australia compare with Japan?," *Journal of Sustainable Urbanization, Planning and Progress*, vol.1, 2016.
- [5] C.-C. Tsai, H.-C. Huang, and S.-C. Lin, "Adaptive Neural Network Control of a Self-Balancing Two-Wheeled Scooter," *IEEE TRANSACTIONS ON INDUSTRIAL ELECTRONICS*, vol. 57, no. 4, pp. 1420-1428, 2010.
- [6] M. Zafar and H. I. Christensen, "Whole Body Control of a Wheeled Inverted Pendulum Humanoid," in Proc. IEEE-RAS 16th International Conference on Humanoid Robots (Humanoids), Cancun, Mexico, 2016: IEEE.
- [7] S.-C. Lin and C.-C. Tsai, "Development of a Self-Balancing Human Transportation Vehicle for the Teaching of Feedback Control," *IEEE TRANSACTIONS ON EDUCATION*, vol. 52, no. 1, pp. 157-168, 2009.
- [8] H. I. Lee, H. W. Kim, and a. S. lung, "Development of a mobile inverted pendulum robot system as a personal transportation vehicle with two driving modes :TransBOT," in Proc. 2010 World Automation Congress, Kobe, Japan, 2010: IEEE.
- [9] Y. Kim, S. H. Kim, and Y. K. Kwak, "Dynamic Analysis of a Nonholonomic Two-Wheeled Inverted Pendulum Robot," *Journal of Intelligent and Robotic Systems*, vol. 44, no. 1, pp. 25-46, 2005.

- [10] P. Frankovsky, L. Dominik, A. Gmiterko, I. Virgala, P. Kurylo, and O. Perminova, "MODELING OF TWO-WHEELED SELF-BALANCING ROBOT DRIVEN BY DC GEARMOTORS," *International Journal of Applied Mechanics and Engineering*, vol. 22, no. 3, pp. 739-747, 2017.
- [11] F. Grasser, A. D'Arrigo, S. Colombi, and A. C. Rufer, "JOE: A Mobile, Inverted Pendulum," *IEEE TRANSACTIONS ON INDUSTRIAL ELECTRONICS*, vol. 49, no. 1, pp. 107-114, 2002.
- [12] O. Boubaker, "The Inverted Pendulum Benchmark in Nonlinear Control Theory: A Survey," *International Journal of Advanced Robotic Systems*, 2013.
- [13] A. Bogdanov, "Optimal Control of a Double Inverted Pendulum on a Cart," OGI School of Science & Engineering, OHSU, Technical Report, CSE-04-006, 2004.
- [14] L. Moysis, "Balancing a double inverted pendulum using optimal control and Laguerre functions," Aristotle University of Thessaloniki, Technical Report, 54124, 2016.
- [15] C. W. Anderson, "Learning to control an inverted pendulum using neural networks," in *IEEE Control Systems Magazine*, vol. 9, no. 3, pp. 31-37, April 1989.
- [16] S. Jung and S. S. Kim, "Control Experiment of a Wheel-Driven Mobile Inverted Pendulum Using Neural Network," in *IEEE Transactions on Control Systems Technology*, vol. 16, no. 2, pp. 297-303, March 2008.
- [17] Shiu-Jer Huang and Chien-Lo Huang, "Control of an inverted pendulum using grey prediction model," in *IEEE Transactions on Industry Applications*, vol. 36, no. 2, pp. 452-458, March-April 2000.
- [18] K. Furuta, M. Yamakita, S. Kobayashi, "Swing-up Control of Inverted Pendulum Using Pseudo-State Feedback," *Proceedings of the Institution of Mechanical Engineers, Part I: Journal of Systems and Control Engineering*, vol. 206, no. 4, 263–269, 1992.
- [19] J. Huang, Z. Guan, T. Matsuno, T. Fukuda and K. Sekiyama, "Sliding-Mode Velocity Control of Mobile-Wheeled Inverted-Pendulum Systems," in *IEEE Transactions on Robotics*, vol. 26, no. 4, pp. 750-758, Aug. 2010.
- [20] J. Chung, H. H. Yoo, "Dynamic analysis of a rotating Cantilever Beam by Using the Finite Element Method," *Journal of Sound and Vibration*, vol. 249, no. 1, 2002.
- [21] J. Cheng , H. Xu A. Yan, "Frequency Analysis of a Rotating Cantilever Beam Using Assumed Mode Method with Coupling Effect," *Mechanics Based Design of Structures and Machines*, vol. 34, no. 1, pp. 25 - 47, 2006.

- [22] P. Wolszczak, K. Łygas, and G. Litak, "Dynamics identification of a piezoelectric vibrational energy harvester by image analysis with a high speed camera," *Mechanical Systems and Signal Processing*, vol. 107, pp. 43-52, 2018.
- [23] M. I. Friswell, S. F. Ali, O. Bilgen, S. Adhikari, A. W. Lees, and G. Litak, "Non-linear piezoelectric vibration energy harvesting from a vertical cantilever beam with tip mass," *Journal of Intelligent Material Systems and Structures*, vol. 23, no. 13, pp. 1505-1521, 2012.
- [24] A. Salehi-Khojin, N. Jalili, and S. N. Mahmoodi, "Vibration analysis of vector piezoresponse force microscopy with coupled flexural-longitudinal and lateral-torsional motions," *Journal of Sound and Vibration*, vol. 322, no. 4-5, pp. 1081-1099, 2009.
- [25] A. N. Ardekany and A. Mehrvarz, "Vibrations Suppression of a Euler-Bernoulli Beam in Contact With a Fluid Using Piezoelectric Actuators," in Proc. 4th International Conference on Robotics and Mechatronics, Tehran, Iran, 2016: IEEE.
- [26] A. Mehrvarz, H. Salarieh, A. Alasty, R. Vatankhah,. (2017). "Vibration boundary control of Timoshenko micro-cantilever using piezoelectric actuators," *Scientia Iranica*, vol. 25, 2017.
- [27] F. A. Ghaith and M. N. Hamdan, "Dynamic Modeling and Control of Elastic Beam Fixed on a Moving Cart", presented at the The 7th Jordanian International Mechanical Engineering Conference (JIMEC'7), Amman, Jordan, 2010.
- [28] M. H. Nguyen, V. T. Ngo, M. T. Nguyen, T. T. H. Le, and V. D. H. Nguyen, "DESIGNING LINEAR FEEDBACK CONTROLLER FOR ELASTIC INVERTED PENDULUM WITH TIP MASS," *Robotica & Management*, vol. 21, no. 2, 2016.
- [29] S. Park, W. K. Chung, Y. Youm and J. W. Lee, "Natural Frequencies and Open-Loop Responses of an Elastic Beam Fixed on a Moving Cart and Carrying an Intermediate Lumped Mass," *Journal of Sound and Vibration*, vol. 230, no. 3, 2000.
- [30] R. N. Banavar and B. Dey, "Stabilizing a Flexible Beam on a Cart: A Distributed Port Hamiltonian Approach," in Proc. European Control Conference 2009, pp. 300-305.
- [31] J. Lin, W.-S. Chao, "Vibration Suppression Control of a BEam-cart System with Piezoelectric Transducers by Decomposed Parallel Adaptive Neuro-fuzzy Control," *Journal of Vibration and Control*, vol. 15, no. 12, pp. 1885-1906, 2009.
- [32] F. Borrelli, *Constrained Optimal Control of Linear and Hybrid Systems*. Springer, 2003.
- [33] E. F. Camacho and C. Bordons, *Model Predictive Control*, 2nd ed. (Advanced Textbooks in Controls and Signal Processing). London, U.K: Springer-Verlag, 2007.

- [34] F. Borrelli, A. Bemporad and M. Morari, *Predictive Control for Linear and Hybrid Systems*. Cambridge University Press, 2017.
- [35] O. Mikulas, "A Framework for Nonlinear Model Predictive Control," Master's of Science, Department of Control Engineering, Czech Technical University in Prague, Prague, 2016.
- [36] C. E. Garcia, D. M. Prett, and M. Morari, "Model Predictive Control: Theory and Practice - a Survey," *Automatica*, vol. 25, no. 3, pp. 335-348, 1989.
- [37] M. Bujarbaruah, X. Zhang, U. Rosolia, and F. Borrelli, "Adaptive MPC for Iterative Tasks," in Proc. 2018 IEEE Conference on Decision and Control (CDC), Miami Beach, FL, USA, 2018.
- [38] T.-D. Chu and C.-K. Chen, "Design and Implementation of Model Predictive Control for a Gyroscopic Inverted Pendulum," *Applied Sciences*, vol. 7, no. 12, pp. 1272-1291, 2017.
- [39] M. Askari, H. A. F. Mohamed, M. Moghavvemi, and S. S. Yang, "Model predictive control of an inverted pendulum," in *2009 International Conference for Technical Postgraduates*, Kuala Lumpur, Malaysia, 2010: IEEE.
- [40] A. Bemporad and M. Morari, "Robust model predictive control: A survey," in *Robustness in identification and control* vol. 245 (Lecture Notes in Control and Information Sciences, 2007, pp. 207-226.
- [41] P. J. Campo and M. Morari, "Robust Model Predictive Control," in Proc. 1987 American Control Conference, Minneapolis, MN, USA, 1987, pp. 1021-1026.
- [42] Z. Q. Zheng and M. Morari, "Robust Stability of Constrained Model Predictive Control," in Proc. 1983 American Control Conference, San Francisco, CA, USA, 1983, pp. 379-383.
- [43] M. V. Kothare, V. Balakrishnan, and M. Morari, "Robust Constrained Model Predictive Control using Linear Matrix Inequalities," *Automatica*, vol. 32 no. 10, pp. 1361-1379, 1996.
- [44] B. Kouvaritakis, J. A. Rossiter, and A. O. T. Chang, "Stable generalised predictive control: an algorithm with guaranteed stability," *IEE Proceedings D - Control Theory and Applications*, vol. 139, no. 4, 1992.
- [45] A. Mehrvarz, M. J. Khodaei, W. Clark, and N. Jalili, "MODELING AND DYNAMICS ANALYSIS OF A BEAM-HOVERBOARD SELF-TRANSPORTATION SYSTEM," in Proc. ASME 2018 Dynamic System and Control Conference, Atlanta, Georgia, USA, 2018: ASME.
- [46] G. James, *Advanced Engineering Mathematics*, 4<sup>th</sup> ed. Essex, U.K., Pearson, 2011.
- [47] "Optimization Problem." Internet: [www.mathworks.com/help/mpc/ug/optimization-problem.html](http://www.mathworks.com/help/mpc/ug/optimization-problem.html) [4/9/19].

- [48] C. Schmid and L.T. Biegler, "Quadratic programming methods for reduced Hessian SQP," *Computers & Chemical Engineering*, Vol. 18, Number 9, 1994, pp. 817–832.
- [49] G.F. Franklin, J.D. Powell, and M.L. Workman, *Digital Control of Dynamic Systems*, Second Edition, Addison-Wesley, 1990.
- [50] A. Alessio and A. Bemporad, (2009) "A Survey on Explicit Model Predictive Control" in *Nonlinear Model Predictive Control. Lecture Notes in Control and Information Sciences*, vol 384. Berlin, Heidelberg: Springer, 2009.